



저작자표시-비영리-변경금지 2.0 대한민국

이용자는 아래의 조건을 따르는 경우에 한하여 자유롭게

- 이 저작물을 복제, 배포, 전송, 전시, 공연 및 방송할 수 있습니다.

다음과 같은 조건을 따라야 합니다:



저작자표시. 귀하는 원저작자를 표시하여야 합니다.



비영리. 귀하는 이 저작물을 영리 목적으로 이용할 수 없습니다.



변경금지. 귀하는 이 저작물을 개작, 변형 또는 가공할 수 없습니다.

- 귀하는, 이 저작물의 재이용이나 배포의 경우, 이 저작물에 적용된 이용허락조건을 명확하게 나타내어야 합니다.
- 저작권자로부터 별도의 허가를 받으면 이러한 조건들은 적용되지 않습니다.

저작권법에 따른 이용자의 권리는 위의 내용에 의하여 영향을 받지 않습니다.

이것은 [이용허락규약\(Legal Code\)](#)을 이해하기 쉽게 요약한 것입니다.

[Disclaimer](#)

이학박사 학위논문

Statistical Analysis on the Turbulent
Multi-scale Interstellar Medium
난류성 다중 규모 성간 물질에 대한 통계 분석 연구

2017 년 2 월

서울대학교 대학원
물리·천문학부 천문학전공
조완기

이학박사 학위논문

Statistical Analysis on the Turbulent
Multi-scale Interstellar Medium
난류성 다중 규모 성간 물질에 대한 통계 분석 연구

2017 년 2 월

서울대학교 대학원
물리·천문학부 천문학전공
조완기

Statistical Analysis on the Turbulent Multi-scale
Interstellar Medium

난류성 다중 규모 성간 물질에 대한 통계 분석 연구

지도교수 구 본 철

이 논문을 이학박사 학위논문으로 제출함

2016 년 12 월

서울대학교 대학원

물리·천문학부 천문학전공

조 완 기

조완기의 이학박사 학위논문을 인준함

2016 년 12 월

위 원 장	_____
부위원장	_____
위 원	_____
위 원	_____
위 원	_____

Statistical Analysis on the Turbulent Multi-scale Interstellar Medium

by

Wankee Cho
(wkcho@astro.snu.ac.kr)

A dissertation submitted in partial fulfillment of the requirements
for the degree of

Doctor of Philosophy

in
Astronomy

in
Astronomy Program
Physics and Astronomy Department
Seoul National University

Committee:

Professor	Woong-Tae Kim
Professor	Bon-Chul Koo
Professor	Yong-Sun Park
Doctor	Jongsoo Kim
Professor	Sung-Chul Yoon

Abstract

Turbulence is ubiquitous in the interstellar medium (ISM) and plays a crucial role in the evolution of the ISM over a large range of scales from AU to kpc. To understand the multi-scale nature of interstellar turbulence, the study of the statistical properties of the interstellar turbulence is required not only for observations but also for numerical simulations. Numerical simulation is the only way to understand the dynamics of interstellar turbulence and is essential for understanding the evolution of turbulent ISM in a variety of different scales and environments. Observational studies also provide a glimpse of nature of interstellar turbulence occurring at various scales based on statistical studies. In this paper, I have conducted statistical analyses of turbulence with observational and numerical studies on the evolution of interstellar turbulence on molecular cloud scale and galactic scale. To do this, I used two well-known statistical methods, the probability density function (PDF) and the power spectrum (PS). In an isothermal or incompressible ideal environment, a typical distribution of the log-normal distribution for PDF and the Kolmogorov power spectrum for PS can be expected.

In the first chapter, I discuss the star formation rate quantitatively in the molecular cloud affected by turbulence and self-gravity. For numerical experiments involving self-gravity, turbulent supersonic flow, and magnetic field, I obtain the density PDF. The density structure of interstellar turbulence deviates from the log-normal distribution by self-gravity. With the investigation of the core formation rate per free fall time, the core for-

mation rate shows a sharp increase with self-gravity. When 100 times of the initial average density is considered as the critical density of the core formation, the core formation rate under the influence of self-gravity is 49 times higher than that of assuming the log-normal distribution. Therefore, the previous study, which assumes the log-normal distribution and has obtained the star formation rate, should be modified to account for self-gravity.

In the second chapter, I present statistical analyses of the stratified and turbulent ISM of numerical models performed on the galactic scale at different vertical distances from the galactic plane. Near the galactic plane, the density PDF shows a double-peaked distribution, indicating a deviation from the log-normal distribution. This double-peaked distribution is due to cold and warm gas components in the ISM. The density PDF of each gas is compared to a log-normal distribution since the gas is assumed to be quasi-mass-conserving with the normalized height by a density-weighted scale height. At higher positions from the galactic plane, warm gas is the majority whose density PDF fits well into the log-normal distribution. The density PS steepens to $-5/3$, and as the velocity PS flattens from $-5/3$ as the positions where I investigated go higher. When the velocity field is divided into compressible and incompressible components, the PS of the incompressible component is flatter compared to the PS of the compressible component. In this study, I devised a new method to visualize the degree of compressibility of the velocity field, which could be calculated in real space with the divergence and curl of the velocity field. It has been expected that powerful explosive phenomena such as supernovae will cause only strong compressive turbulence around. But from the way of visualizing compressibility, it can be shown that incom-

pressible components are caused by curved shock waves near supernova remnants.

In the third chapter, I present a study on the turbulent interstellar medium from neutral hydrogen distributed in the Outer spiral arm using I-GALFA HI 21 cm survey data. The slope of PS is steeper ($\alpha \sim -2$) at lower latitudes than at higher latitudes ($\alpha \sim -1.8$). Near the galactic plane, the slope gradually increases with the thickness of the velocity channel and falls (-1.97) as the thickness reaches the thermal velocity of the medium. To understand this change in slope, I compare the I-GALFA observations with numerical models. I synthesized a position-position-velocity cube from a numerical model with similar surface density. From the cube, I found that the effect of young supernova remnants can be one possibility to cause a change in the slope of the PS for the integrated brightness temperature. The PDFs of the integrated brightness temperature do not fit log-normal distribution. Near the galactic plane, it was skewed to the low-density region and skewed toward the higher-density region. And these PDFs are well divided into two log-normal distributions, each representing cold and warm components of neutral hydrogen.

Keywords: turbulence — ISM: clouds — ISM: atoms — ISM: kinematics and dynamics — ISM: structure — stars: formation — Galaxy: structure — methods: numerical — hydrodynamics — magnetohydrodynamics — methods: statistical — radio lines : ISM

Student Number: 2006-30123

Contents

Abstract	i
Chapter 1 Introduction	1
1.1 Overview on Interstellar Turbulence	1
1.1.1 Interstellar Turbulence in the Ideal Environment . .	3
1.1.2 Realistic Interstellar Turbulence	6
1.2 Motivation and Outline of the Thesis	8
Bibliography	11
Chapter 2 Enhanced Core Formation Rate in a Turbulent Cloud by Self-gravity	15
2.1 Introduction	15
2.2 Numerical Method	17
2.3 Results	20
2.4 Discussions and Conclusions	32
Bibliography	34
Chapter 3 Statistical Properties of the Turbulent, Strat- ified, Two-phase ISM	37

3.1	Introduction	37
3.2	Methods	42
3.2.1	Numerical Simulations	42
3.2.2	Analysis Methods	49
3.3	Results	52
3.3.1	Density Probability Distribution Function	52
3.3.2	Power Spectra of Density and Velocity	63
3.3.3	Measurement of the Compressibility in Real Space	66
3.4	Discussion	73
3.4.1	Relation between the Mass-weighted Mean and Dispersion of Density	73
3.4.2	Relationship between RMS Sonic Mach Number and Statistics	76
3.5	Summary	79
	Bibliography	81

**Chapter 4 Statistical Properties in the Outer Spiral Arm
in the I-GALFA HI 21 cm Line Survey 85**

4.1	Introduction	85
4.2	Observations	89
4.3	Results	96
4.3.1	Density Power Spectra	96
4.3.2	Density Probability Distribution Function	101
4.4	Power Spectra from a Synthetic HI PPV Cube	105
4.4.1	Numerical Simulations	105
4.4.2	Slopes of Power Spectra of the Synthetic Cubes	105
4.5	Summary	111

Bibliography	113
Chapter 5 Convulsion	116
초록	121
Acknowledgements	124

List of Figures

Figure 2.1	Three-dimensional volume renderings of two density fields	19
Figure 2.2	Evolution of the volume fractions of density PDFs	21
Figure 2.3	CFR _{ff} with time evolution	24
Figure 2.4	One-dimensional velocity dispersion as a function of box size	26
Figure 2.5	Increase of core mass fraction with time in different critical densities	31
Figure 3.1	Horizontally averaged densities as a function of the vertical distance and time	46
Figure 3.2	Time-averaged mass fractions of the model QA10	48
Figure 3.3	Time-averaged mass fractions of (a) volume density and (b) column density of the model QA10 .	53
Figure 3.4	Time-averaged mass fractions of density PDFs with cold and warm gas	56
Figure 3.5	Time-averaged means, dispersions, and skewnesses of the density PDFs	58

Figure 3.6	Rms sonic Mach number and the mass fraction of cold phase gas with height	61
Figure 3.7	Time-averaged power spectra of density and velocity field, and compressive and solenoidal components of the velocity field of model QA10 . . .	65
Figure 3.8	A snapshot for the ratio of compressibility and time-averaged compressibility ratio	67
Figure 3.9	The sliced images of the compressibility	70
Figure 3.10	The relationship between rms sonic Mach number and velocity compressibility	72
Figure 3.11	Relations between time-averaged means and dispersions	75
Figure 3.12	Relationship between Mach number and dispersions	78
Figure 4.1	The integrated (l, v) maps of the Outer spiral arm and Scutum-Centaurus arm	91
Figure 4.2	The averaged brightness temperature	94
Figure 4.3	Logarithm of longitude-averaged brightness temperature	95
Figure 4.4	Averaged power spectra of brightness temperature distributions	98
Figure 4.5	One-dimensional velocity profiles and their Gaussian fits at the lower latitudes	100
Figure 4.6	Probability distribution function of the integrated brightness temperature	102
Figure 4.7	Brightness temperature maps from the synthetic HI PPV cube	108

Figure 4.8 Slopes of the power spectra at the different latitudes of the synthetic HI PPV cube 110

List of Tables

Table 3.1	Model Parameters and Key Results from K13	. . .	44
-----------	---	-------	----

Chapter 1

Introduction

1.1 Overview on Interstellar Turbulence

The interstellar medium (ISM) is highly turbulent. Turbulence is one of the important physical ingredients of the ISM, which builds complicated structures of the ISM, influences star/core formation rate, generates magnetic fields, accelerates cosmic-ray particles and so force. Turbulence is manifested by random, nonlinear motion over many scales. The nonlinear nature of the turbulence allows complex structures to form and plays a significant role in the process of energy circulation in the ISM. In other words, turbulence makes large-scale coherent eddies which interact each other to create smaller eddies and transfers the kinetic energy from a large to a smaller scale. While the kinetic energy of turbulence is transferred to the smaller scales, the turbulent structures fragment into the smaller substructures avoiding the global collapse. On a small scale, the convergent flow generated by turbulence makes transient, clumpy and

complicated structures inside a molecular cloud (MC) with local gravitational collapse to enhance star/core formation (e.g., Bonazzola et al. 1987[2]; Vázquez-Semadeni et al. 1995[32]). In this process, eddies of each scale appear to be self-similar, scale-invariant. This scale-invariant property has been shown as a scaling relation between MC size and internal velocity (Larson 1981[30]), where the observed MCs are dominated by supersonic turbulence, as the internal velocity of the MCs is greater than the thermal dispersion. In the HI observations of our galaxy and Small Magellanic Cloud (SMC), the turbulent ISM is seen whose density structure is shaped like a flocculent cloud (Elmegreen and Scalo 2004[10]).

Turbulence affects the evolution of the ISM in the inertial range. The extent of the turbulent activity in the ISM covers from kpc to AU, as seen in Armstrong's 'Big Power Law in the sky' (Armstrong et al. 1995[2]). In fact, most of the ISM is affected by interstellar turbulence. The inertial range refers to the driving scale from which energy is injected to the dissipation scale where the kinetic energy of turbulence is converted into thermal energy. Dissipation may be caused by molecular viscosity at the smallest scale, or by ambipolar diffusion of the ISM (Zweibel and Josafatsson 1983[51]; Zweibel and Brandenburg 1997[50]). On a smaller scale than the dissipation scale, turbulence is no longer important. The driving scale depends on each driving source. The mechanism by which the driving source injects energy and causes turbulence is not yet known in detail. The types of driving sources can be divided into two broad categories according to Mac Low and Klessen (2004)[29]. The first category is stellar sources such as supernovae explosions, stellar winds of massive stars, and an expanding HII region. Especially, a supernova (SN) explosion is the most energetic astronomical phenomenon in the galaxy. Since

its energy is 10^{51} ergs, and the explosion period is 50 yr per a Type II SN, even if only a few % of supernova explosive energy, it is the primary driving source of interstellar turbulence. Avillez and Breitschwardt (2007)[3] calculated the scale of the turbulence driven by the SNe explosions as a correlation length by a two-point correlation function in galactic-scale numerical calculations. The longitudinal correlation length of the blast wave is about 70 pc, twice the length of the transverse correlation, which is equivalent to roughly isotropic interstellar turbulence. At the sites of low star formation rate (SFR), galactic spiral shocks, various instabilities on a galactic scale such as magnetic-rotational instability, gravitational scattering by massive cloud complexes, and interaction between galaxies can be strong driving sources. All these driving sources produce turbulence that is larger than MCs. Therefore, numerical experiments of interstellar turbulence on MCs are causing the driving scale to be larger and isotropic than the computational domain. But for the diffuse ISM, the driving scales are smaller than or comparable to the galactic scale to be no more isotropic.

1.1.1 Interstellar Turbulence in the Ideal Environment

Numerical experiments have been used as a necessary and unique tool, to understand the dynamics of turbulence. Furthermore, because of the complexity of large and small structures made by turbulence, I can use statistical analysis to gain insight into the nature of interstellar turbulence as well as the evolution of the turbulent ISM. The representative statistical analysis tools for the turbulent ISM are probability distribution function (PDF) and power spectrum (PS). The PDF shows the density distribution of the turbulent medium at a glance and expresses the properties

of turbulence. Lots of pure hydrodynamic simulations have been carried out for supersonic and isothermal turbulence in a small scale computational box, following the early simulations of Bania and Lyon (1980)[4], Passot et al. (1988)[35], and Porter et al. (1999)[39]. The statistical analysis of those simulations has presented that the density PDF of turbulent medium follows a lognormal (LN) distribution as a result of the central limit theorem (Vázquez-Semadeni 1994[31]),

$$P(\ln(\rho)) = \frac{1}{\sqrt{2\pi\sigma^2}} \exp\left[-\frac{(\rho - \mu)^2}{2\sigma^2}\right], \quad (1.1)$$

where P is the probability of density ρ , μ is the mean, and σ is the standard deviation of the density in the medium. On a large scale, Wada and Norman (2001)[48] have conducted galaxy-scale numerical simulations involving interstellar turbulence and have shown that the density PDF approaches the log-normal distribution.

In terms of density PDF, one of the most important aspects of interstellar turbulence in a small scale range is that it is related to star formation. The classical star formation theory is based on a strong magnetic field and ambipolar diffusion, which successfully explained the low SFR of MCs. The essential part of the theory is that the magnetic field is strong enough to support the gravitational collapse of an MC. The magnetic field strengths measured through mostly the Zeeman splitting method in MCs is not always high enough. An alternative star formation theory is based on turbulence in MCs, which in fact doesn't require strong magnetic field strength. Based on the LN-PDF of the turbulent ISM, core/star formation rates and core or stellar initial mass functions are measured (Padoan & Nordlund 2002[25]; Krumholz & McKee 2005[16]; Elmegreen 2008[5]; Hennebelle & Chabrier 2008[10]). Krumholtz and McKee (2005)[16] mea-

sured the SFR per free fall time in an MC from the numerical models and found the rate increase with the higher sonic Mach number.

In the view of energy flow, PS is another important statistical tool. Larson (1981)[30] found the power-law correlations between cloud sizes and linewidths on a small scale. From theory, it is known that the power index of velocity PS in the turbulent medium follows Kolmogorov's PS (Kolmogorov 1941[18]), where the PS of energy for the incompressible turbulent medium is shown to be $E(k) \sim k^{-5/3}$. In the shock-dominated area, the power index increases to -2 . The PS of density in the ISM has been found to be close to Kolmogorov's, too. For HI emission, Crovisier and Dickey (1983)[4] first reported that their PS could be explained by the Kolmogorov spectrum. Since then, power spectra of interstellar turbulence have been obtained and compared with the Kolmogorov spectrum using many different kinds of observations: HI emission and absorption, CO emission, and infrared in Our Galaxy, SMC and Large Magellanic cloud (Green 1993[19]; Dickey et al. 2001[6]; Miville-Deschênes et al. 2003[32]; Deshpande et al. 2000[9]; Stutzki et al. 1998[43]; Plume et al. 2000[38]; Bensch et al. 2001[5]; Gautier et al. 1992[15]; Schlegel et al. 1998[40]; Stanimirović et al. 1999[41]; Stanimirović et al. 2000[42]; Klessen 2000[17]; Elmegreen and Staveley-Smith 2001[12]).

In summary, on a small scale, interstellar turbulence has assumed an ideal condition such as supersonic, isothermal, and incompressible. (1) The isothermality of interstellar turbulence makes the density PDF follow the LN distribution. (2) Supersonic turbulence can broaden the PDF width and promote star formation locally in high-density regions. (3) Turbulent flow in an incompressible medium causes the power index of PS to have the same. However, the interstellar turbulence is being dealt with

in a more realistic environment, where it is free from the ideal conditions assumed in the previous studies. Besides, since the cores produced by turbulence locally are transient, it 's hard to generate stars from them.

1.1.2 Realistic Interstellar Turbulence

To understand the evolution of the ISM better, it is not possible only with interstellar turbulence. We should consider a more realistic interstellar environment. Statistical analysis shows the environmental effect on turbulence. In other words, we can confirm the effect from the n -th order moment of the density PDF of the turbulent ISM. First, the larger the sonic Mach number of the turbulence, the greater the variance or standard deviation, the second moment of the density PDF. Also, skewness, the third moment of the density PDF, changes with the polytropic index in the nonisothermal environment. Depending on the compressibility of the turbulence, the shape of the density PDF may change (Federrath et al. 2008[8]). The compressible forcing makes the density PDF broader and more skewed negatively than the density PDF by incompressible forcing. Since the diffuse ISM has been discussed on a larger scale than the MC scale, the scale of turbulence caused by stellar sources such as supernovae may be comparable to or less than that of the diffuse ISM. However, if compressible turbulence also interacts with the magnetic field, the density PDF of the ISM can again approximate the LN distribution (Molina et al. 2012[23]). The density PDF of the nonisothermal, compressible, turbulent ISM is still close to the LN distribution.

The density PDF is out of the LN distribution when self-gravity acts on the turbulent medium. Self-gravity will collapse a high-density gas to cores and eventually form a star (Klessen 2001[25]). In the process of the

star formation, Vázquez-Semadeni et al. (1995)[32] found that the density PDF deviates from the LN distribution with numerical simulations of the turbulent ISM that interacts with self-gravity. Their density PDF is obtained by adding a power-law tail in a high-density region to the LN distribution. Kainulainen et al. (2009)[12] also investigated the density PDF of active star-forming MCs and, as a result, found the non-LN distributions with extended tails similar to that of Vázquez-Semadeni et al. (1995)[32]. These tails are known to be observational evidence of the self-gravity. Such a non-LN distribution will also affect the SFR because it has been calculated assuming the LN distribution. However, there is no study on how much SFR varies in the turbulent medium due to the self-gravity. Since self-gravity increases the probability of high-density region, SFR can also be expected to increase.

Studies on interstellar turbulence on a large scale require a more realistic interstellar turbulence model. For example, our galaxy disk consists of a thin disk of a cold medium and a thick disk of a warm medium. Gazol and Kim (2013)[11] numerically investigated the density PDF according to the sonic Mach number in a two-phase medium and reported that each medium is separated and follows the LN distribution. Since the fraction of the cold/warm medium will vary with the galactic latitude, the density PDF can be expected to change. In observation, Berkhuijsen and Fletcher (2008)[1] interpreted skewed PDFs in the Galactic HI emission in the way of separating them into two LN-PDFs for cold and warm gas components of the turbulent ISM. Sonic Mach number would vary with the latitude, too, since the temperature increases from the galactic plane to the higher latitude. Also, the compressibility of the medium would be different between the galactic midplane and the high latitude region, because su-

pernova explosions would compress the circumstellar medium around the galactic midplane. On the contrary, if energy injection is performed at the galaxy scale due to galactic spiral shock or magnetic-rotational instability in the outer region of the galaxy where the SFR and the frequency of the supernova explosion are low, the change of sonic Mach number according to the latitude of the galaxy may not be significant.

Previous studies on interstellar turbulence have focused less on galactic-scale turbulence due to lack of computational power and so forth, although large-scale turbulence could show relationships with the other physical ingredients or with a more realistic environment, collectively. Numerous numerical simulations of interstellar turbulence have been designed, and even if there were galaxy-scale numerical experiments, they were only interested in large-scale structures such as bubbles, worms, a galactic disk, and spiral arms. Those structures are formed by the galactic-scale turbulence, self and external gravity, magnetic fields, cooling, background or dynamical heating, and so on (Avillez 2000 [3]; Wada and Norman 2001[48]; Wada et al. 2002[46]; Wada and Norman 2007[47]; Joung and Mac Low 2006[19]; Tasker and Bryan 2006[40]; Kritsuk et al. 2010[26]; Gent et al. 2013[12]; Kim et al. 2013[16]). Large-scale structures of the ISM are very turbulent in the widespread HI high-resolution survey from observation, so statistical studies on interstellar turbulence on galaxy scale are needed.

1.2 Motivation and Outline of the Thesis

In the previous section, typical characteristics of interstellar turbulence are introduced. These statistical properties, however, undergo changes

when additional physical ingredients are involved in the turbulent medium. I tried to understand how the statistical properties of interstellar turbulence modify in a more realistic environment and thus evolve the ISM through scale. In this thesis, at a small scale, I will represent the effects of interstellar turbulence and self-gravity on the evolution of the ISM such as SFR numerically, and then from this, I could understand the theory of star formation by interstellar turbulence more brightly. On a galaxy scale, I try to understand the characteristics of interstellar turbulence in a more realistic environment, assuming a two-phase medium of cold and warm components, containing various physical ingredients. Synergetic studies involving numerics and observations have helped to understand turbulence better. Here, the statistical analysis of galactic HI observation and comparisons with the numerical results are aimed to understand the characteristics of the galactic scale turbulent ISM.

In Chapter 2 of this thesis, I focused on density PDFs enhanced by self-gravity in a small-scale MC. The previous studies show that the self-gravity makes the density PDF deviate from LN-distribution and helps turbulence increase the SFR. Our research will show how much the SFR will be enhanced in the turbulent ISM after turning-on self-gravity from a numerical simulation. In Chapter 3, on a larger scale, I will describe the structure of the turbulent and stratified ISM as a function of the vertical height from the galactic plane using numerical simulations and observed HI emission data cube. It is expected that the statistical properties of the turbulence will be altered along the vertical distance because sonic Mach number, compressibility, the fraction of the cold and the warm neutral gas, and so on are varied as a function of the vertical distance. In this thesis, the numerical models in Kim et al. (2013)[16] are analyzed statis-

tically. The models have very extensive coverage of the vertical direction, realistic conditions such as heating and cooling processes, self- and external gravity, and realistic SN-driven forcing. I will provide a detailed description of the model and its turbulence properties in the chapter. In Chapter 4, HI 21 cm survey data from the Inner Galaxy Arecibo L-band Feed Array (I-GALFA) (Peek et al. 2010[28]; Peek et al. 2011[29]; Koo et al. 2010[19]; Gibson et al. 2012[13]) will be used to study on the Outer spiral arm in the first quadrant of the Milky Way. We, moreover, compare the statistical properties of observational results to those of the synthetic PPV cube from a galactic-scale numerical simulation (Kim et al. 2013[16]). The comparison enables us to understand that the variation of spectral slope as a function of the velocity channel width. The summary of the thesis will be followed, in Chapter 5.

Bibliography

- [1] Armstrong, J. W., Rickett, B. J., & Spangler, S. R. 1995, *ApJ*, 443, 209
- [2] Avillez, M. 2000, *MNRAS*, 315, 479
- [3] Avillez, M. & Breitschwerdt, D, 2007, *ApJ*, 665, 35
- [4] Bania, T. M., & Lyon, J. G., *ApJ*, 557, 451
- [5] Bensch, F., Stützk, J., Ossenkopf, V., 2001, *A&A*, 366, 636
- [6] Berkhuijsen, E., & Fletcher, A. 2008, *MNRAS*, 390, 19
- [7] Bonazzola, S., Heyvaerts, J., Falgarone, E., Perault, M., & Puget, J. L., 1987, *A&A*, 172, 293
- [8] Crovisier, J., & Dickey, J. M., 1983, *A&A*, 122, 282
- [9] Deshpande, A. A., Dwarakanath, K. S., & Goss, W. M., 2000, *ApJ*, 543, 227
- [10] Dickey, J. M., McClure-Griffiths, N. M., Stanimirović, S., Gaensler, B. M., & Green, A. J., 2001, *ApJ*, 561, 264

- [11] Elmegreen B. G., 2008, *ApJ*, 672, 1006
- [12] Elmegreen, B.G., Kim, S., & Staveley-Smith, L., 2001, *ApJ*, 548, 749
- [13] Elmegreen, B. G., & Scalo, J. 2004, *ARA&A*, 42, 211
- [14] Federrath, C., Klessen, R. S., & Schmidt, W. 2008, *ApJ*, 688, 79
- [15] Gautier, T. N., Boulanger, F., Perault, M., & Puget, J. L., 1992, *AJ*, 103, 1313
- [16] Gazol, A. & Kim, J., 2013, *ApJ*, 765, 49
- [17] Gent, F. A., Shukurov, A., Sarson, G. R., Fletcher, A., & Mantere, M. J. 2013, *MNRAS*, 435, 689
- [18] Gibson, S. J., Koo, B., Douglas, K. A., et al. 2012, *BAAS*, 219, 349.29
- [19] Green, D. A., 1993, *MNRAS*, 262, 327
- [20] Hennebelle P., Chabrier G., 2008, *ApJ*, 684, 395
- [21] Joung, M. K. R., & Mac Low, M.- M., 2006, *ApJ*, 653, 1266
- [22] Kainulainen J., Beuther H., Henning T., Plume R., 2009, *A&A*, 508, L35
- [23] Kim, C-G., Ostriker, E. C., & Kim, W-T 2013, *ApJ*, 776, 1
- [24] Klessen, R. S., 2000, *ApJ*, 535, 869
- [25] Klessen, R. S., 2001, *ApJ*, 556, 837
- [26] Kolmogorov, A. 1941, *DoSSR*, 30, 301
- [27] Koo, B.-C., Gibson, S. J., Kang, J.-h., et al. 2010, *HiA*, 15, 788

- [28] Kritsuk, A. G., Usyugov S. D., & Norman, M. L., 2011, IAUS, 270, 179
- [29] Krumholz M. R., McKee C. F., 2005, ApJ, 630, 250
- [30] Larson, R. B. 1981, MNRAS, 194, 809
- [31] Mac Low, M.- M., & Klessen, R. S., 2004, RvMP, 76, 125
- [32] Miville-Deschênes, M.- A., Levrier, F., & Falgarone, E., 2003, ApJ, 593, 831
- [33] Molina, F. Z., Glover, S. C. O., Federrath, C., & Klessen, R. S., 2012, MNRAS, 423, 2680
- [34] Padoan P., Nordlund A., 2002, ApJ, 576, 870
- [35] Passot, T., Pouquet, and Woodward., P., 1988, A&A, 197, 228.
- [36] Peek, J. E. G., Begum, A., Douglas, K. A., et al. 2010, in ASP Conf. Ser. 438, The Dynamic Interstellar Medium: A Celebration of the Canadian Galactic Plane Survey, ed. R. Kothes, T. L. Landecker, & A. G. Willis (San Francisco, CA: ASP), 393
- [37] Peek, J. E. G., Heiles, C., Douglas, K. A., et al. 2011, ApJS, 194, 20
- [38] Plume, R., Bensch, F., Howe, J. E., Ashby M. L. N., & Bergin, E. A., et al., 2000, ApJ, 538, 133
- [39] Porter, D., Pouquet, A., Sytine, I., & Woodward, P., 1999, Physica A 263, 263
- [40] Schlegel, D. J., Finkbeiner, D. P., & Davis, M., 1998, ApJ, 500, 525

- [41] Stanimirović, S., Staveley-Smith, L., Dickey, J. M., Sault, R.J., & Snowden, S. L., 1999, MNRAS, 302, 417
- [42] Stanimirović, S., Staveley-Smith, L., van der Hulst, J. M., Bontekoe, T. J. R., Kester, D. J. M., & Jones, P. A., 2000, MNRAS, 315, 791
- [43] Stutzki, J., Bensch, F., Heithausen, A., Ossenkopf, V., & Zielinsky, M., 1998, A&A, 336, 697.
- [44] Tasker, E. j., & Bryan G. L., 2006, ApJ, 641, 878
- [45] Vázquez-Semadeni, E., 1994, ApJ, 423, 681
- [46] Vázquez-Semadeni, E., Passot, T., & Pouquet, A., 1995, ApJ, 441, 702
- [47] Wada, K., Meurer, G., & Norman, C. A., 2002, ApJ, 577, 197
- [48] Wada, K., & Norman, C. A., 2001, ApJ, 547, 172
- [49] Wada, K., & Norman, C. A., 2007, ApJ, 660, 276
- [50] Zweibel, E. G., & Brandenburg, A., 1997, Astrophys. J. 478, 563
- [51] Zweibel, E. G., & Josafatsson, K., 1983, Astrophys. J. 270, 511

Chapter 2

Enhanced Core Formation Rate in a Turbulent Cloud by Self-gravity

2.1 Introduction

¹ Probability distribution functions (PDFs) for volume and column density fields calculated from turbulence simulations with the isothermal equation of state have been successfully fitted on a log-normal (LN) distribution (Vázquez-Semadeni 1994[31]; Padoan et al. 1997[34]; Passot & Vázquez-Semadeni 1998[27]; Nordlund & Padoan 1999[24]; Ostriker et al. 1999[25]; Ostriker et al. 2001[26]; Vázquez-Semadeni & Garcá 2001[31]; [15]; Lemaster & Stone 2008[19]; Federrath et al. 2008b[7]). In addition to these numerical works, it has been recently reported that the H α emission measurement for the warm ionized medium (Hill et al. 2008[11]) and the densities of the diffuse ionized gas and diffuse atomic gas (Berkhuijsen

¹This paper is published in the MNRAS, 2011, 410, L8-L12

& Fletcher 2008[1]) follow the LN distribution. It is now believed that a LN density (or column density) PDF is regarded as the signature of turbulence in an isothermal medium.

In the field of star formation theories based on turbulence, the LN density PDF has also become one of important ingredients. The analytical models of Padoan & Nordlund (2002)[25] and Hennebelle & Chabrier (2008)[10] predicted stellar initial or core mass functions, whose mass distributions at lower masses are largely determined by the LN density PDF. Elmegreen (2002)[4] and Elmegreen (2008)[5] used the LN density PDF in order to calculate the cumulative mass fraction above a critical number density ($> 10^5 \text{ cm}^{-3}$), which is directly related to the star formation efficiency. Krumholz & McKee (2005)[16] also measured dimensionless star formation rate per free-fall time based on the LN density PDF. Instead of picking up a specific value of a critical density as in Elmegreen (2002)[4] and Elmegreen (2008)[5], they determined it by equating the local Jeans and sonic lengths.

The numerical simulations mentioned in the first paragraph step forward with self-gravity of gas. It is easily expected that the inclusion of self-gravity in a turbulent simulation results in a density PDF with an extended tail at higher densities due to the very nature of self-gravity, which has been, in fact, reported in a few literatures. With self-gravity, Klessen (2000)[17] showed the extended tails of density PDFs from his decay and driven hydrodynamic simulations, Dib & Burkert (2005)[5] also reported that in a density PDF from one of their numerical models, and Federrath et al. (2008a)[6] showed the tail at high-density region in their density PDFs using tracer particles with self-gravity. Finally, Vázquez-Semadeni et al. (2008)[33] performed self-gravitating, isother-

mal, hydrodynamic simulations and showed progressive increase of the volume fraction of density PDFs at high densities as a function of time.

The motivation of this paper is to show quantitatively how much core formation rates in a turbulent cloud can be increased by self-gravity with respect to that measured from a LN density PDF. As we mentioned above, density PDFs from isothermal simulations without self-gravity results in LN functions. Dense filaments formed in those simulations are transient, which reside in the high end of the functions. It is self-gravity that enables some of them to develop into collapsing cores and helps the cores accrete nearby gas at later evolutionary stages. With this motivation, we perform a numerical simulation for core formation in a self-gravitating, magnetically supercritical, supersonically turbulent, isothermal cloud. We show that the volume fractions of density PDFs at higher densities are increasing as time goes on. Even though the increments of the volume fractions at high densities over a LN distribution are small, those of the mass fractions are quite large due to the very high densities. This, in fact, leads to the significant increment of the core (star) formation rate compared with the one measured from the LN density PDF.

2.2 Numerical Method

In order to see the formation and evolution of cores in a turbulent cloud, we numerically integrate the MHD equations with an isothermal equation of state and the Poisson's equation, using a MHD code based on a total variation diminishing scheme (Kim et al. 1999[13]) and a gravity solver based on the fast Fourier transform. As an initial condition, a uniformly magnetized medium is assumed in a rectangular box. The periodic boundary condition is imposed in each direction of the box. The

combined isothermal MHD and Poisson's equations are scale-free, and can be written in a dimensionless form with two parameters. One is the plasma beta, β , the ratio of gas to magnetic pressures, and the other is the Jeans number, J , the ratio of the length of one side of the computational box, L , to the initial Jeans length, $\lambda_{J0} = (\pi a_s^2 / G \rho_0)^{1/2}$, where a_s is an isothermal sound speed, G is the gravitational constant, and ρ_0 is an initial density.

We basically follow the recipes for turbulence generation in Stone et al. (1998)[28] and Mac Low (1999)[18]. Velocity fluctuations are generated in a Fourier space with the same functional form of the velocity power spectrum in Stone et al. (1998)[28]. We, however, take the peak wavenumber, $2(2\pi/L)$, which is larger than their choice. We then transform the fluctuations into a real space, and adjust their amplitudes in a way that an input kinetic energy rate is a constant. The level of turbulence driven by this method can be parameterized by a rms (root-mean-square) sonic Mach number, M_s . We start a driven turbulence simulation without turning on the self-gravity, and wait until a converged turbulent flow is developed. Then, we turn on self-gravity of gas, where turbulence has been generated continuously, and set the time to zero.

Numerical simulations based on the above-mentioned method with different parameters have been done. From those simulations, some results on lifetimes of cores (Vázquez-Semadeni et al. 2005a[33]; Galván-Madrid et al. 2007[9]), core formation efficiency (Vázquez-Semadeni et al. 2005b[34]), virial balance of cores (Dib et al. 2007[3]), and molecular line profiles of a core (Lee & Kim 2009[17]) have been reported. In this work, we reuse data from one of 512^3 simulations with parameters, $\beta = 0.1$, $J = 4$, and $M_s = 10$.

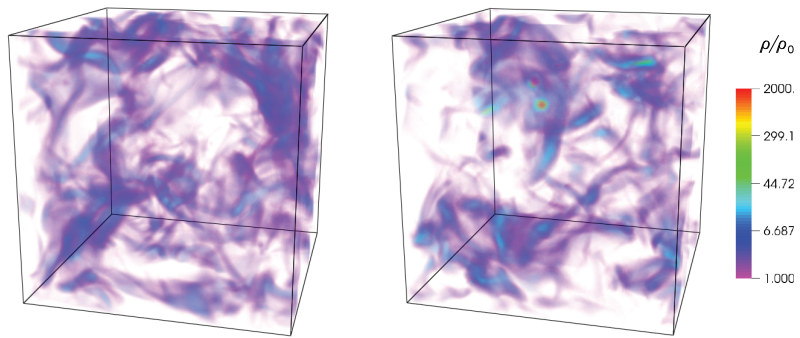


Figure 2.1 Three-dimensional volume renderings of two density fields at $t/t_{\text{ff}} = 0.0$ (left) and $t/t_{\text{ff}} = 1.8$ (right), respectively, where t_{ff} is the free-fall time with an initial density. The evolutionary time is set to zero when self-gravity is on. Colors in a bar is mapped onto density values that are normalized with an initial value, ρ_0 .

2.3 Results

The series of volume rendering images of three-dimensional density fields are made for visualizing the evolution of density fields as a function of time. Two of them are shown in Fig. 2.1. The left image shows a density field at time just before turning on self-gravity of gas, $t/t_{\text{ff}} = 0$, where $t_{\text{ff}} = \sqrt{3\pi/32G\rho_0} = \sqrt{3/32}(\lambda_{J0}/a_s)$, the free-fall time with the mean density inside the computational box. A color bar in the rightmost side represents a mapping between colors and densities normalized with an initial or a mean value. The color bar only covers a normalized density range from 1 to 2000, which enables us to see the distribution of high density gas more clearly. There are many dense filaments in the left image. These are formed by the interaction of large-scale supersonic flows with sonic Mach number around 10. Isothermal shocks along a field line easily increase the normalized densities at post shock regions up to 100, which is the square of the Mach number. After turning on self-gravity of gas, some of these filaments increase their central densities either by merging each other or accreting nearby gas. Several condensations are seen in red or yellow colors in the right image at $t/t_{\text{ff}} = 1.8$, whose normalized central densities are larger than about 300. In fact, they are the main contributors to form bumps raised on top of a LN density PDF at high densities (see Fig. 2.2), which are eventually evolved into collapsing cores.

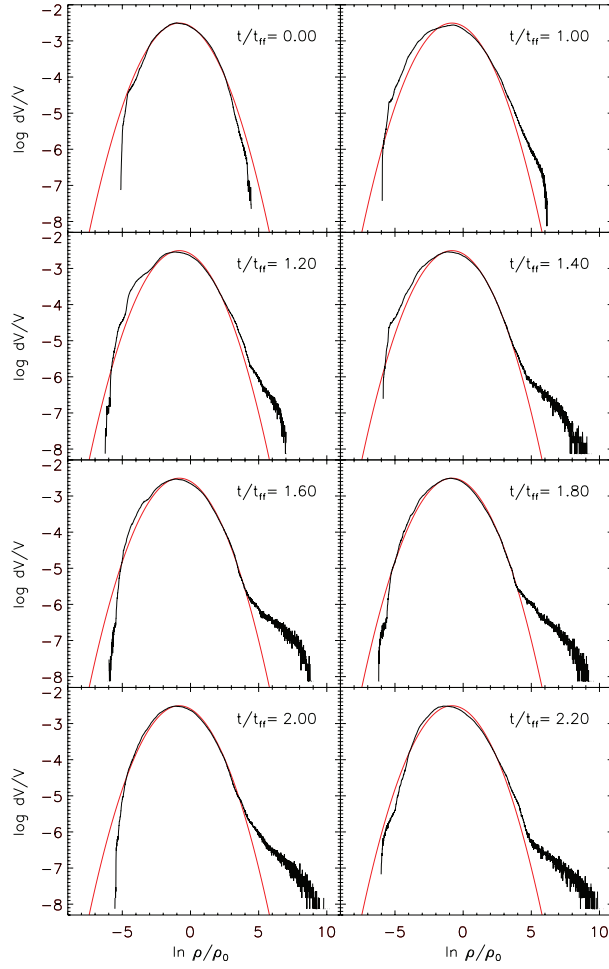


Figure 2.2 Evolution of the volume fractions of density PDFs. The horizontal and vertical axes are logarithmic values based on e and 10, respectively. A black line in each panel is a density PDF in a computational box at a specified time in units of initial free-fall time. A red line is a fit of a density PDF averaged over the saturated stage of turbulence before turning on self-gravity with a LN distribution, equation (2.1). The fitted parameters are $\mu = -0.82$ and $\sigma = 1.28$. The same red line is plotted in each panel.

We plot two kinds of density PDFs in black and red lines in each panel of Fig. 2.2. The horizontal and vertical axes represent the natural logarithm of the normalized density and the logarithmic value based on 10 of volume fractions, respectively. The PDFs in black are calculated from density fields from our numerical simulation at different times. The time information normalized with the initial free-fall time is put at the upper right corner at each panel. The red lines at each panel are the same from a fit on an averaged density PDF over a saturated turbulent state before turning on self-gravity taken over from $t/t_{\text{ff}} = -1.3$ to $t/t_{\text{ff}} = 0.0$, where the number of density fields used in the average is 50 with a LN distribution,

$$p_{\text{LN}}(s) = \frac{1}{\sqrt{2\pi\sigma^2}} \exp\left[-\frac{(s-\mu)^2}{2\sigma^2}\right], \quad (2.1)$$

where $s = \ln(\rho/\rho_0)$, μ is the mean, and σ is the standard deviation. Since mass has not added into or subtracted from the computational box during our simulation, total mass inside the box is conserved. The conservation constraint at the initial state and a state where the density PDF is described with the LN distribution like, $\int_{-\infty}^{\infty} \rho_0 \delta(s) ds = \int_{-\infty}^{\infty} \rho p_{\text{LN}}(s) ds$, provides us a relation, $\mu = -\sigma^2/2$ (Passot & Vázquez-Semadeni 1998[27]), where $\delta(s)$ is a Dirac-delta function with the peak at s_0 of the initial density. This reduces the two parameters, μ and σ , in equation (2.1) into one. The mean value of the averaged density PDF, $p(s)$, is -0.82 calculated from $\sum_i s_i p(s_i)$, where s_i is a discrete value of s , and $p(s_i)$ is a volume fraction at s_i . A LN distribution with $\sigma = 1.28$ calculated from the relation $\sigma = \sqrt{(-2)\mu}$ is plotted in each panel as a red line. It serves as a fiducial line to see how much a black line at each panel deviates from the LN distribution. Later, we will also use the σ value to estimate a core formation rate per free-fall time based on the LN distribution.

A black line in the panel at $t/t_{\text{ff}} = 0.0$ shows a density PDF at the turn-on time of self-gravity. It is quite well matched with the red line except at low and high density end. These deviations from LN distribution is due to the finite numerical resolution in our simulation and the intermittency effects of the turbulence with solenoidal and compressible forcing (Kritsuk et al. 2007[15]; Federrath et al. (2010[12])). Those can make core mass fraction lower in some degree at the high density ends even with self-gravity. This shape of density PDFs, as time goes on, is hardly changed from the LN distribution up to around $t/t_{\text{ff}} = 1.0$ since it takes nearly one free-fall time (t_{ff}) for self-gravity to exercise its control over supersonic turbulent flows. So we choose several time steps with equi-time interval, $\delta t = 0.2t_{\text{ff}}$, after one free-fall time. Then, self-gravity makes significant change in density PDFs shown in Fig. 2.2 along the black lines. Self-gravity makes the bump, quite an excess of volume fractions at a high density tail, raised rapidly up to $t/t_{\text{ff}} = 1.4$. The bump height is almost saturated afterwards. Even though the excess volume fractions over the LN distribution is small, the excess mass fractions should be quite significant due to high densities at the bump. This excess mass fractions contribute significantly to core formation rates calculated in the followings. We can see the same trace shown by core mass fraction with time, which is discussed briefly later with Fig. 2.5.

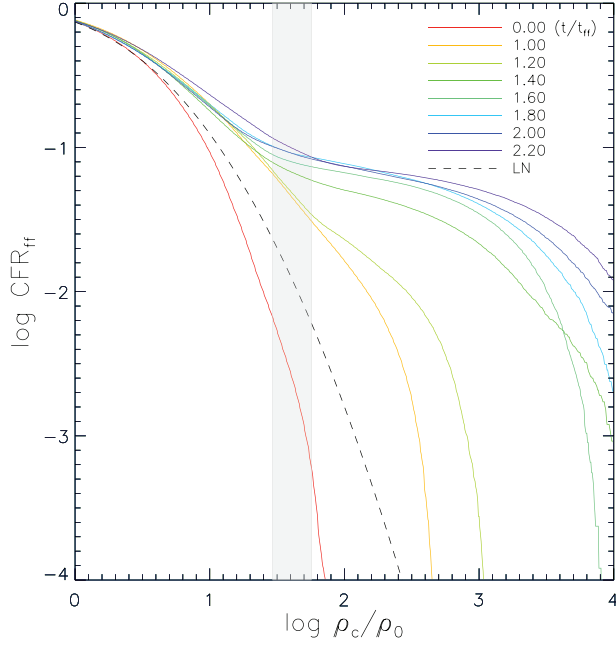


Figure 2.3 CFR_{ff} with time evolution, which is measured from the cumulative mass fractions as a function of the normalized density. Solid lines with different colors are calculated by integrating equation (2.2) numerically with the density PDFs at different times shown in Fig. 2.2, respectively. A dash line denotes the LN distribution, which is from equation (2.3) with $\sigma = 1.28$. And the gray region covers over $\rho_c/\rho_0 = 31 \sim 48$, where the local Jeans length equals sonic length

We calculate the cumulative mass fractions of the density fields above a certain density threshold. Since the volume fraction of a density PDF at each time is known, the cumulative mass fraction, $f(s)$, of gas whose density is larger than s is easily calculated using the following equation,

$$f(s) = \int_s^\infty \frac{\rho}{\rho_0} p(s) ds = \int_s^\infty e^s p(s) ds. \quad (2.2)$$

If $p(s)$ is replaced with equation (2.1) with the relation $\mu = -\sigma^2/2$, the integration results in

$$f_{\text{LN}}(s) = \frac{1}{2} \left[1 + \operatorname{erf} \left(\frac{\sigma^2 - 2s}{2\sqrt{2}\sigma} \right) \right], \quad (2.3)$$

which is the same as the expression for CFR_{ff} in equation (20) for in Krumholz & McKee (2005)[16], with $\epsilon_{\text{core}} = 1$, $\phi_t = 1$ simply; CFR_{ff} at a certain time means the mass fraction that will be condensed into core during the next t_{ff} . Then, we numerically integrate equation (2.2) with $p(s)$'s shown in Fig. 2.2 and plot CFR_{ff} curves as a function of $\log(\rho/\rho_0)$ in Fig. 2.3 where a dashed line is calculated from equation (2.3) with $\sigma = 1.28$. A red line at $t/t_{\text{ff}} = 0.0$ lies below the dashed line. This is due to the fact that, in Fig. 2.2, the density PDF at $t/t_{\text{ff}} = 0.0$ drawn with a black line has smaller volume fractions at high densities than the red line. As time goes on, the CFR_{ff} increases significantly at high densities. Expected from Fig. 2.2, the increasing rate is high during the rapid development of the bump before the saturation. Since the saturation, the CFR_{ff} curves are significantly higher than the one calculated from the LN distribution, which is totally due to self-gravity.

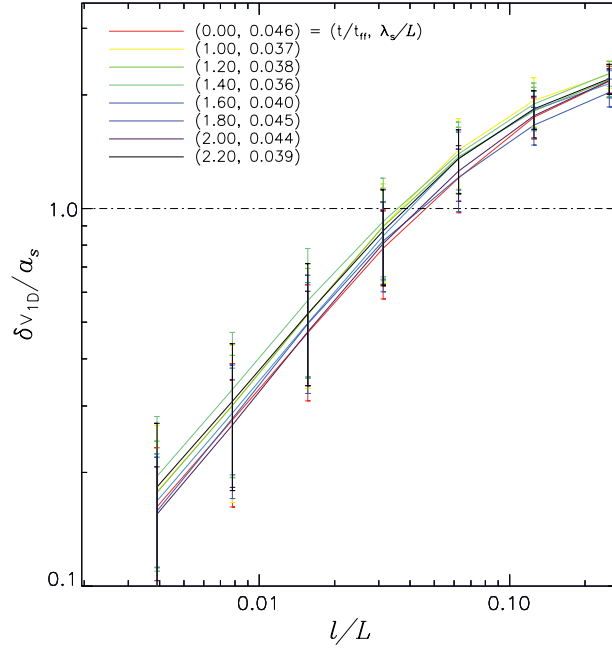


Figure 2.4 One-dimensional velocity dispersion as a function of box size. Normalization units for the dispersion and the size are the isothermal speed a_s and the one-dimensional size L of the computational box, respectively. For a given time, measured mean values of velocity dispersions at different box sizes are connected, and the standard deviations are plotted with error bars. The normalized times t/t_{ff} and measured, normalized sonic lengths λ_s/L are given in parentheses.

To quantitatively compare core formation rate under self-gravity effect with that from the LN distribution, we need proper definition of critical density for the gravitational collapse of gas against turbulence. One idea that has been used is to compare a local Jeans length, $\lambda_J = (\pi a_s^2 / G \rho)^{1/2}$, and a sonic length, λ_s (Padoan 1995[23]; Vázquez-Semadeni et al. 2003[32]; Krumholz & McKee 2005[16]). In fact, the condition of $\lambda_J = \lambda_s$ gives a critical density ρ_c normalized with the initial density,

$$\frac{\rho_c}{\rho_0} = \left(\frac{\lambda_{J0}}{\lambda_s} \right)^2, \quad (2.4)$$

where λ_{J0} is the initial Jeans length. The physical background of this condition is that a transonic turbulent velocity dispersion over a volume defined by λ_s is barely able to support gravitational collapse of the gas inside the volume. Since $\lambda_{J0} = L/4$, which is given as an initial condition, we need λ_s in terms of L for the critical density. For the calculation of λ_s , we follow the method in Vázquez-Semadeni et al. 2003[32]. We take 100 random positions in the computational box, put a same-sized box less than L centered at each position, and calculate one-dimensional velocity dispersions of turbulent velocity fields in the 100 boxes. Fig. 2.4 shows the velocity dispersions normalized with the isothermal sound speed as a function of a normalized box size. The dispersions at eight different times are plotted with colored solid lines, where error bars at the measured box size are included, even though they are hardly distinguished with each other. A horizontal dash-dot line with a unit normalized velocity dispersion is drawn. In fact, sonic lengths are determined at the meeting points of the dash-dot line and solid lines. The measured sonic lengths at different time steps are included in the figure, which are in the range, $0.036L \lesssim \lambda_s \lesssim 0.046L$. If $\lambda_{J0} = L/4$ are plugged in equation (2.4) with

this range of λ_s , then the critical density is converted to be $31 \lesssim \rho_c/\rho_0 \lesssim 48$. It is above the range that gas collapses into core by self-gravity to be counted into CFR_{ff} .

Now we compare the CFR_{ff} with self-gravity to the theoretical value from LN density distribution with equation (2.3) in the above critical density range. First, we can measure the theoretical CFR_{ff} at a certain time from equation (2.3). For example, when t/t_{ff} is 1.6, the critical density ρ_c/ρ_0 is 39 and from the equation CFR_{ff} is measured in 0.013. In the other hand, the CFR_{ff} is 0.079 measured at the above critical density, 39, in Fig. 2.3, which is 6 times larger than the theoretical value from the LN distribution. Like this way, CFR_{ff} s are nearly 4.1 times larger than those without self-gravity while the bump in Fig. 2.2 grows rapidly to $t/t_{\text{ff}} < 1.4$. The ratios of CFR_{ff} with self-gravity to the theoretical CFR_{ff} become larger to be 6.1 averaged from $1.4 \lesssim t/t_{\text{ff}}$. The argument based on the local Jeans and sonic lengths, however, may not give a correct critical density for measuring the core formation rate of our numerical simulation. Because the normalized critical density defined from this manner just means that turbulence can scatter core with the the same power of gravitational collapse, it is not guaranteed for the gas to collapse actually. Considering the fact that an instant density jump brought by a Mach 10 isothermal shock along a magnetic field line is around 100, the range of the critical density can be attained by shocks only. Thus the density of gas collapsed into core purely by self-gravity may be at least above 100 times denser than ρ_0 . If we set the normalized critical density as 100 at $t/t_{\text{ff}} = 1.8$, for example, the CFR_{ff} with gravity becomes 49 times larger than the one from LN density PDF. Also there is uncertainty from the growth of artificial fragments (Truelove et al. 1997[29]) in the measure-

ment of core formation rate, which can increase the maximum density. Furthermore, we must consider the magnetic field plays a certain role in supporting cores. But these give little effect on measuring CFR_{ff} because we just cumulate the mass fraction over a certain criterion that is far lower than the maximum density.

We plot core mass fraction curves with time of the several different critical densities in Fig. 2.5, which equals core formation rate in our definition based on Krumholz & McKee (2005)[16]. Because of the reason given in the previous paragraph, we choose a rather wide range of critical densities normalized with the initial density, from 30 to 300. The time is again normalized by the free-fall time with the initial density. The lines colored in red and green show more or less constant levels up to around $t/t_{\text{ff}} = 1.0$. There is very tiny fraction of the total mass, whose normalized density is larger than 100. This is due to the fact that it takes self-gravity around one free-fall time to exercise its control over turbulent flows, in which the density PDF cannot deviate from the LN distribution. After that point, the core formation rate increases rapidly up, which is the transition phase for adjusting the self-gravity. This rapid increase of the fractions is mostly due to accretion of nearby gas onto several cores, as we have seen in the PDF plots (Fig. 2.2 and Fig. 2.3). Also we can see that it takes the gravity to adjust fully longer transient time from $t/t_{\text{ff}} = 1.0$ to 1.6 with the higher critical density. In the final state, the self-gravity settles down and increases slowly.

Padoan & Nordlund (2009)[26] described the time evolution of star formation efficiency, which equals the evolution of the core mass fraction curves in our Fig. 2.5. They said CFR_{ff} was measured by the least-square fitting on the CFE curves. But this is the increasing rate of CFR_{ff} in our

definition. We can estimate this increasing rate in Fig. 2.5 following their argument for the estimation only after transient epoch, after $t/t_{\text{ff}} = 1.6$ at the higher critical density in our experiment. In Fig. 2.5, we can see that the higher critical density is, the lower increasing rate becomes. This is because turbulence can supply gas to the outside of core in the global scale but scatter gas inside of the core at the local scale whereas self-gravity accretes the gas into core continuously. We should mention that we didn't include feedback processes from the stars that might form in our simulation. Without the processes core formation efficiency eventually approaches one. However, at least, before the formation of a first star in the simulation, our measurement of the core formation efficiency is quite right. In order to properly measure the core formation efficiency, especially, at the later evolutionary state of a molecular cloud, one should include the feedback processes in a simulation.

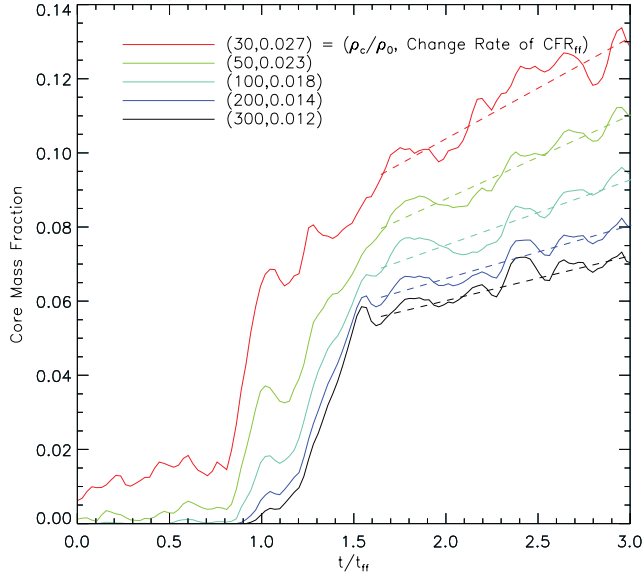


Figure 2.5 Increase of core mass fraction with time in different critical densities. The core formation efficiency is defined as a fraction of total mass in the computational box, whose density is larger than a critical density. The time is measured in units of free-fall time with an initial density. The critical density, ρ_c , is normalized with the initial density, ρ_0 . The results of least-square fitting for the lines, CFR_{ff} , are shown in dashed lines and also legend.

2.4 Discussions and Conclusions

Recently, Kainulainen et al. (2009)[12] catalogued column density PDFs of 23 molecular cloud complexes from the 2MASS archive. They classified them into two groups based on star formation activity and compared their column density PDFs. The column density PDFs of star-forming clouds always have extended tails, whereas the PDFs of clouds without active star formation follow LN distributions or a bit excess at high column densities. Furthermore, the cumulative fractions of column density PDFs with star-forming clouds are significantly larger than those without active star formation. These observational results clearly show that self-gravity plays a role in forming the extended tails of the PDFs, which is consistent with our work.

We remind that the extended tails of density PDFs at high densities from isothermal simulations with self-gravity have been shown in a few previous literatures. However, they haven't been taken seriously partially due to the very small increase of volume fractions over LN distributions. As we have clearly and quantitatively shown in the result section, it is the small increase of the volume fraction that can enhance the core formation rate per free-fall time quite significantly. Cores in a turbulent cloud cannot form without self-gravity. Core (star) formation rates or core (stellar) mass functions should be measured in the context of a self-gravitating cloud. Therefore, it is likely that core formation rates previously measured based on the LN density PDF (Krumholz & McKee 2005[16]; Elmegreen 2008[5]) are underestimated. Likewise, the core or stellar initial mass functions based on the LN distribution (Padoan & Nordlund 2002[25]; Hennebelle & Chabrier 2008hen08) need to be modi-

fied.

We performed a magnetically supercritical and supersonic turbulence simulation with the isothermal equation of state to study the effects of self-gravity on density PDFs and the core formation rate. Here are conclusions from the study. First self-gravity helps to form the extended tail of a density PDF at high densities, which significantly increase the core formation rate per free-fall time. Second, the normalized critical density for core collapse determined by the equal condition between the local Jeans and sonic lengths is $31 \lesssim \rho_c/\rho_0 \lesssim 48$. In this range of critical density, CFR_{ff} is 6.1 times larger than that from the LN distribution (Krumholz & McKee 2005[16]). Third, because above critical density range is smaller than 100, a density jump brought by an isothermal Mach 10 shock in our simulation, the determined critical density may not give a correct condition for the core formation. For a given normalized critical density, 100, the core formation rate per free-fall time becomes about 49 times larger. Therefore, self-gravity plays a significant role in enhancing the core formation rate per free-fall time. Fourth, the increment of CFR_{ff} is described with time. The change rate is smoother when the critical density is higher because turbulence scatters the gas inside of core whereas self-gravity accretes the gas continuously.

Bibliography

- [1] Berkhuijsen E. M., Fletcher A., 2008, MNRAS, 390, L19
- [2] Dib S., Burkert A., 2005, ApJ, 630, 238
- [3] Dib S., Kim J., Vázquez-Semadeni E., Shadmehri, M., 2007, ApJ, 661, 262
- [4] Elmegreen B. G., 2002, ApJ, 577, 206
- [5] Elmegreen B. G., 2008, ApJ, 672, 1006
- [6] Federrath, C., Glover, S. C. O., Klessen, R. S., & Schmidt, W. 2008a, Physica Scripta T, 132, 014025
- [7] Federrath C., Klessen R. S., Schmidt, W., 2008, ApJ, 688, L79
- [8] Federrath, C., Roman-Duval, J., Klessen, R. S., Schmidt, W., & Mac Low, M.-M. 2010, A&A, 512, A81
- [9] Gálvan-Madrid R., Vázquez-Semadeni E., Kim J., Ballesteros-Paredes J., 2007, ApJ, 670, 480
- [10] Hennebelle P., Chabrier G., 2008, ApJ, 684, 395

- [11] Hill A. S., Benjamin R. A., Kowal G., Reynolds R. J., Haffner M., Lazarian, A., 2008, *ApJ*, 686, 363
- [12] Kainulainen J., Beuther H., Henning T., Plume R., 2009, *A&A*, 508, L35
- [13] Kim J., Ryu D., Jones T. W., Hong S. S., 1999, *ApJ*, 514, 506
- [14] Klessen R. S., 2000, *ApJ*, 535, 869
- [15] Kritsuk A. G., Norman M. L. Padoan P., Wagner, R., 2007, *ApJ*, 665, 416
- [16] Krumholz M. R., McKee C. F., 2005, *ApJ*, 630, 250
- [17] Lee J., Kim J., 2009, *ApJ*, 699, L108
- [18] Mac Low M.-M., 1999, *ApJ*, 524, 169
- [19] Lemaster M. N., Stone J. M., 2008, *ApJ*, 682, L97
- [20] Nordlund A., Padoan P., 1999, in Franco J., Carraminana A., eds., *Interstellar Turbulence*, p. 218
- [21] Ostriker E. C., Gammie C. F., Stone, J. M., 1999, *ApJ*, 513, 259
- [22] Ostriker E. C., Stone J. M., Gammie C. F., 2001, *ApJ*, 546, 980
- [23] Padoan P., 1995, *MNRAS*, 277, 377
- [24] Padoan P., Nordlund A., Jones B. J. T., 1997, *MNRAS*, 288, 145
- [25] Padoan P., Nordlund A., 2002, *ApJ*, 576, 870
- [26] Padoan P., Nordlund A., 2009, *ApJL*, arXiv0907.0248P

- [27] Passot T., Vázquez-Semadeni E., 1998, *Phys. Rev. E*, 58, 4501
- [28] Stone J. M., Ostriker E. C., Gammie C. F., 1998, *ApJ*, 508, L99
- [29] Truelove, J. K., Klein, R. I., & McKee, C. F. et al. 1997, *ApJ*, 489, L179
- [30] Vázquez-Semadeni, E., 1994, *ApJ*, 423, 681
- [31] Vázquez-Semadeni E., Garcá N., 2001, *ApJ*, 557, 727
- [32] Vázquez-Semadeni E., Ballesteros-Paredes J., Klessen R. S., 2003, *ApJ*, 585, L131
- [33] Vázquez-Semadeni E., Kim J., Shadmehri M., Ballesteros-Paredes J. 2005, *ApJ*, 618, 344
- [34] Vázquez-Semadeni E., Kim J., Ballesteros-Paredes J. 2005, *ApJ*, 630, L49
- [35] Vázquez-Semadeni E., González R. F., Ballesteros-Paredes J., Gazol A., Kim J., 2008, *MNRAS*, 390, 769

Chapter 3

Statistical Properties of the Turbulent, Stratified, Two-phase ISM

3.1 Introduction

Turbulence is ubiquitous in the interstellar medium (ISM). It interacts with the entities of the ISM such as gas, dust, cosmic-ray particles, and magnetic and gravitational fields.

One of the important consequences of the interaction is that turbulence modulates the star formation rate (SFR) in molecular clouds. On small scales, turbulence increases the SFR by generating convergent flows where cores and stars are more likely formed by the help of self-gravity. On large scales, turbulence acts like pressure preventing a global gravitational collapse of a molecular cloud (e.g., Bonazzola et al. 1987[2]; Vázquez-Semadeni et al. 1995[32]).

Observed power spectra of the interstellar turbulence have a continu-

ous power-law distribution with high power at larger scales and low power at smaller scales. Motivated by the classical Kolmogorov turbulence theory (Kolmogorov 1941[18]), people believe that the energy of the turbulence is mostly injected at large scales, cascades toward smaller scales, and eventually dissipates at tiny dissipation scales (see, Armstrong et al. 1995[2]; Vázquez-Semadeni et al. 2000[44]; Larson 2003[27]; Elmegreen and Scalo 2004[10]; Mac Low and Klessen 2004[29]; Chepurnov and Lazarian 2010[7]). However, the energy of turbulence is supplied not only by stellar origins such as stellar winds, supernova remnants (SNRs), and superbubbles at small scales but also by the galactic rotation on large scales. Small-scale turbulence could also be excited by cosmic rays with streaming instability (Wentzel 1968[48]), where the shock amplification by an SNR in the turbulent ISM might be substantial (Balsara, Benjamin and Cox 2001[4], and by other instabilities (Hall 1980[17]). It is still unclear which driving source is the most dominant one for the interstellar turbulence and how the energy of the turbulence is transferred from large scales to smaller scales.

Turbulence properties have been described by statistical methods such as the probability distribution function (PDF) and power spectrum (PS). The density PDFs (dPDFs) of simulated turbulent flows show a lognormal (LN) distribution when the flows are in an isothermal state (Vázquez-Semadeni 1994[31]; Ostriker et al. 1999[25]; Klessen 2000[17]; Ostriker et al. 2001[26]; Li et al. 2004[22]). When a dPDF follows the LN-distribution, the relationship between the dispersion of the density and the sonic Mach number is known as,

$$\sigma^2 = \ln(1 + b^2 M_s^2) \quad (3.1)$$

where σ^2 is the dispersion of the logarithm of the volume density, M_s is

the root-mean-square (rms) sonic Mach number, $M_s = \langle v_{rms} \rangle / \langle \sigma \rangle$, and b is a constant related to the compressibility of a forcing velocity field (Padoan et al. 1997[34]; Passot and Vázquez-Semadeni 1998[27]; Federrath et al. 2008[8]; Price et al. 2011[36]). However, the shape of a dPDF and the $\sigma - M_s$ relation are dependent upon physics included in numerical simulations. We here mentioned several previous papers that have addressed this issue. The dPDFs of the non-isothermal turbulent flows have power-law tails (Passot and Vázquez-Semadeni 1998[27]; Scalo et al. 1998[30]; Nordlund and Padoan 1999[24]). The inclusion of magnetic fields into isothermal hydrodynamic turbulent flows lowers, for a given Mach number, the dispersion of the density in equation (3.1) (Molina et al. 2012[23]). The inclusion of self-gravity in an isothermal turbulence simulation makes a dPDF deviated from the LN-distribution and, in fact, enhances the fraction of the dPDF at a high-density region (Klessen 2000 [17]; Dib and Berkert 2005[5]; Federrath et al. 2008[8]; Vázquez-Semadeni et al. 2008[33]; Cho and Kim 2011[3]). This enhancement results in a higher SFR in a molecular cloud than the one measured without the self-gravity (Cho and Kim 2011[3]). The nature of forcing to generate turbulence changes the shape of a dPDF (Federrath et al. 2008[8]): the pure solenoidal (incompressible) forcing in a turbulence simulation leads a dPDF to have an LN-distribution whereas the pure compressive forcing makes the shape of a dPDF wider and more negatively skewed.

Density and velocity power spectra are the other useful statistical quantities to analyze the properties of turbulence flows. Their power-law slopes reflect certain properties of turbulent flows. For example, the power index $-5/3$ is well-known from the Kolmogorov theory for an incompressible turbulent flow (Kolmogorov 1941[18]). The velocity power

index in shock-dominated turbulent flows steepens to become -2 . Therefore it is expected that velocity power indexes of compressible turbulence flows should be in between -2 and $-5/3$. On the other hand, Kim and Ryu (2005)[15] found the density PS flattens with increasing rms sonic Mach number in their numerical models for isothermal hydrodynamic turbulent flows, while the velocity PS steepens (Gazol and Kim 2010[10]).

Almost all of the previous works have used forcing generated artificially in Fourier space, which is quite different from forcing based on astrophysical origins. They have also done numerical simulations in a uniform density background. In a realistic ISM environment, the driving force of turbulence caused by astrophysical objects such as supernovae occurs in real space and the influence region of supernovae goes far beyond from the midplane. In this paper, we use results from the numerical simulations which incorporate multi-phase gas, supernovae, and self-gravity of the gas in a vertically stratified medium under the influence of the externally given Galactic gravitational field. What is new in this work compared with other works is that we investigate density and column density PDFs, and density and velocity PS as a function of the vertical distance from the midplane.

This paper attempts to show the characteristics of the interstellar turbulence in the stratified ISM with the PDFs and power spectra. Galactic-scale numerical simulations on the turbulent ISM have been done (Avillez 2000[3]; Joungh and Mac Low 2006[19]; Tasker and Bryan 2006[40]; Wada et al. 2002[46]; Wada and Norman 2007[47]; Agertz et al. 2009[1]; Kritsuk et al. 2010[26]; Gent et al. 2013[12]; Kim et al. 2013[16]). But the simulations focus more on the evolution of galactic structures such as a galactic disk, spiral arms, and worms. The statistical properties of the

turbulent and stratified interstellar medium have not been fully understood. The primary goal of this paper is to investigate the statistical quantities of the PDF and PS as a function of height from the galactic midplane. In fact, the dPDF near the midplane does not follow the LN-distribution anymore. It, however, shows double-peak shape because of the influence of self-gravity and cooling. We could see the change of the slopes of the power spectra with height, where density PS steepens with increasing height while velocity PS flattens. We also propose a new equation to calculate the compressibility of a velocity in real space and apply this equation to see the compressibility in our numerical box. From the visualization of the new equation, we could see that SNe not only generate the compressible velocity component by strong shocks themselves but also the solenoidal velocity component by the propagation of curved shocks.

We organize the paper in the following way. In section 2, we briefly describe the numerical models in Kim et al. (2013)[16] and introduce the analysis methods that we are going to use. We present results on the dPDFs, PS and the compressibility of velocity fields in section 3. In section 4, we will discuss on the correlations among density dispersion, density mean, velocity compressibility, and rms sonic Mach number in section 4. Summary in Section 5 will be followed.

3.2 Methods

3.2.1 Numerical Simulations

We need the numerical simulations with (a) realistic physical ingredients including self and external gravities, cooling and heating processes for the thermal instability, (b) a realistic driving source of turbulence by SN explosions, and (c) quite large vertical coverage compared to a scale height to properly describe the vertically stratified ISM. The models of Kim et al. (2013)[16] (hereafter, K13) are satisfied with our needs to study statistical properties of the turbulent and stratified ISM.

We refer the reader to K13 for full descriptions of their hydrodynamic (HD) models, methods, and evolutions. Here, we briefly summarize the models we use in this paper. We use full three-dimensional models of the QA-series among the numerical models of K13, where the gas surface density varies from 2.5 to 20 $M_{\odot} \text{ pc}^{-2}$. In Table 1, we summarize the model parameters and key numerical outcomes for this series. The density of stars plus dark matter, ρ_{sd} , parameterizes the external gravity as $g_{\text{ext}} = -4\pi G \rho_{\text{sd}} z \hat{z}$. $\rho_{\text{sd}} \propto \Sigma^2$ to keep stellar Toomre Q parameter constant. t_{orb} is the orbital period, $t_{\text{orb}} \equiv 2\pi/\Omega = 220\text{Myr}(\Sigma/10M_{\odot}\text{pc}^{-2})^{-1}$, where the galactic rotational speed varies as $\Omega = 28\text{kms}^{-1}\text{kpc}^{-1}(10M_{\odot} \text{ pc}^{-2}/\Sigma)$ to keep the gaseous Toomre Q parameter constant. The vertical domain size, L_z , varies to enclose at least two scale height of two-phase gas. The horizontal domain sizes are $L_x = L_y = 512 \text{ pc}$ and the resolution of each grid is fixed by 2 pc in all models. The HD simulations solve the hydrodynamic equations in a local three-dimensional shearing box using Athena code (Stone et al. 2008[38]; Stone and Gardiner 2009[39]). The surface density for star formation rate is presented as a result to compare

to the surface density at second column. Violent SN activity may lower the star formation rate. For guessing the turbulent state of the ISM, vertical turbulent and thermal velocity dispersions are shown in the last columns. We could see the turbulence is around transonic from those columns.

The models include optically-thin cooling, self- and external gravities, galactic differential rotation, and star formation feedback in the forms of momentum injection by supernovae (SNe) and time-varying heating rates. When a self-gravitating cloud forms and becomes denser than a density threshold for star formation, SN feedback is assigned stochastically based on the local expected star formation rates at that density with the efficiency per free-fall time of 1%. SN feedback is realized in the form of expanding SN remnant (SNR) with a fixed total momentum of $p_* = 3 \times 10^5 M_\odot \text{km/s}$, consistent to the final momentum conserving stage of a radiative SNR (e.g., Thornton et al. 1998[41]; Kim and Ostriker 2015[23]). The initial size of a supernova remnant has a radius of 10 pc. Although, by assuming all the SNe as in the momentum conserving stage, the hot ISM cannot be produced by SN feedback in the simulations for simplicity. Many properties of warm and cold phases of gas ($T \leq 10^4$ K) are consistent with observations (e.g., Kim et al. 2014[22]).

Table 3.1. Model Parameters and Key Results from K13

Model	Σ ($M_{\odot}\text{pc}^{-2}$)	ρ_{sd} ($M_{\odot}\text{pc}^{-3}$)	t_{orb} (Myr)	L_z (pc)	$\log \Sigma_{\text{SFR}}^{\text{a}}$ ($M_{\odot}\text{kpc}^{-2}\text{yr}^{-1}$)	v_z^{b} (kms^{-1})	v_{th}^{b} (kms^{-1})
QA02	2.5	0.0031	878	2048	-4.11 ± 0.32	4.33 ± 1.07	4.07 ± 0.57
QA05	5.0	0.0125	439	1024	-3.43 ± 0.27	5.03 ± 1.00	3.85 ± 0.78
QA10	10.0	0.0500	219	512	-2.82 ± 0.12	4.67 ± 0.47	4.11 ± 0.26
QA20	20.0	0.2000	146	256	-2.18 ± 0.06	5.05 ± 0.32	4.47 ± 0.22

^aSFR surface density

^bVertical turbulent and thermal velocity dispersions of the diffuse gas

In Fig. 3.1, we show the horizontally-averaged density as a function of vertical distance and time. The time is normalized by t_{orb} . The solid line represents the density-weighted scale height, $H_n(t)$,

$$H_n(t) = \left[\frac{\int z^2 \bar{n}(t, z) dz}{\int \bar{n}(t, z) dz} \right]^{1/2} \quad (3.2)$$

where $\bar{n}(t, z)$ is the horizontally-averaged number density along the vertical direction at a given time t . The distribution \bar{n} and $H_n(t)$ show a nearly periodic oscillation, which is mainly due to self-regulation cycles of star formation. With enhanced star formation rates, stronger SN feedback and higher heating rate puff the disk up. This makes the ISM thermally and dynamically warmer to reduce SFRs. Less SN feedback and lower heating rate shrink the disk back to be ready for next star formation events. The entire disk responds together to the cycles because the heating rate is spatially constant. The time scale of this oscillation is well described by the have of free-particle crossing time in the vertical direction, $t_{\text{osc}} \approx 0.5(\pi/G\rho_{\text{sd}})^{1/2}$ or $t_{\text{osc}}/t_{\text{orb}} = 0.27$ (see K13). One of the primary purposes of this paper is to see the statistical properties of turbulence at different vertical distances. For a fair comparison of properties with similar background conditions, we use the normalized vertical distance at each time, $z'(t) = z/H_n(t)$. We take $z' = 2$ as a maximum vertical distance and make a comparison of statistical properties at that normalized vertical distance.

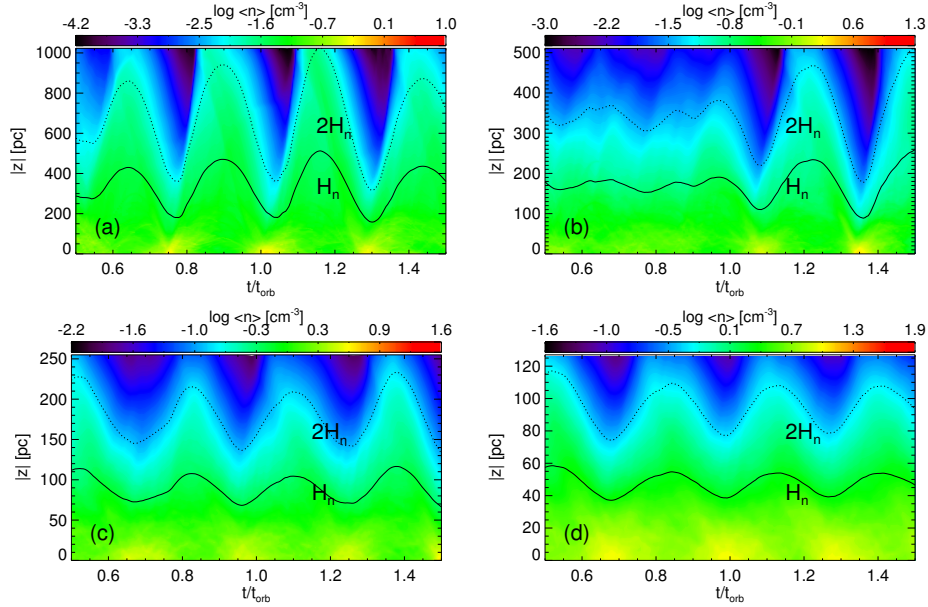


Figure 3.1 Horizontally averaged densities as a function of the vertical distance and time of the models, QA02 (a), QA05 (b), QA10 (c) and QA20 (d). The rainbow color bars represent the averaged densities in a logarithmic scale. Solid and dotted lines delineate the density weighted scale heights of each model, H_n as a function of time. The averaged densities and the scale heights show that the thickness of the disk is quasi-periodically changing.

Fig. 3.2 presents the mass fractions of gas at four different heights on a density-pressure plane. The time-averaged mass fractions are shown at four specific heights of 0, 0.4, 0.8, and 1.2 as the representative values of different heights. And the fractions are colorized with a rainbow color table. In each plot, we draw blue and red lines on the locus of thermal equilibrium with $\langle \Gamma \rangle = 0.61\Gamma_0$ and $T = 10^{2.9}$ K, respectively. The significant fraction of the gas is on and near the blue line in each plot, and the gas could be separated into cold (below the red line) and warm (above the red line) phases by phase transition temperature, $T_{\text{pt}} = 10^{2.9}$ K. At low heights, $z' = 0$ and 0.4 in Fig. 3.2, we could see that the cold phase overwhelming the warm phase, since relatively high-density gas by the external and self-gravities cools down efficiently. As the height increases to higher latitudes, $z' = 0.8$ and 1.2, the dominant phase of gas moves from the cold phase to warm phase. In fact, most of the gas resides the warm phase in the low-density region following the thermal equilibrium line in Fig. 3.2. What is interesting in these plots of Fig. 3.2 is that the warm phase seems to be in a quasi-isothermal state. The part of the solid blue line in the low-density region ($\log n_H \leq 0$) is nearly parallel to the dashed line with the fixed temperature; $T = 10^{2.9}$ K. The gas at the warm phase mostly distributes along the blue line below the low-density region at each panel. So the warm phase seems to be in the quasi-isothermal state along the equilibrium curve.

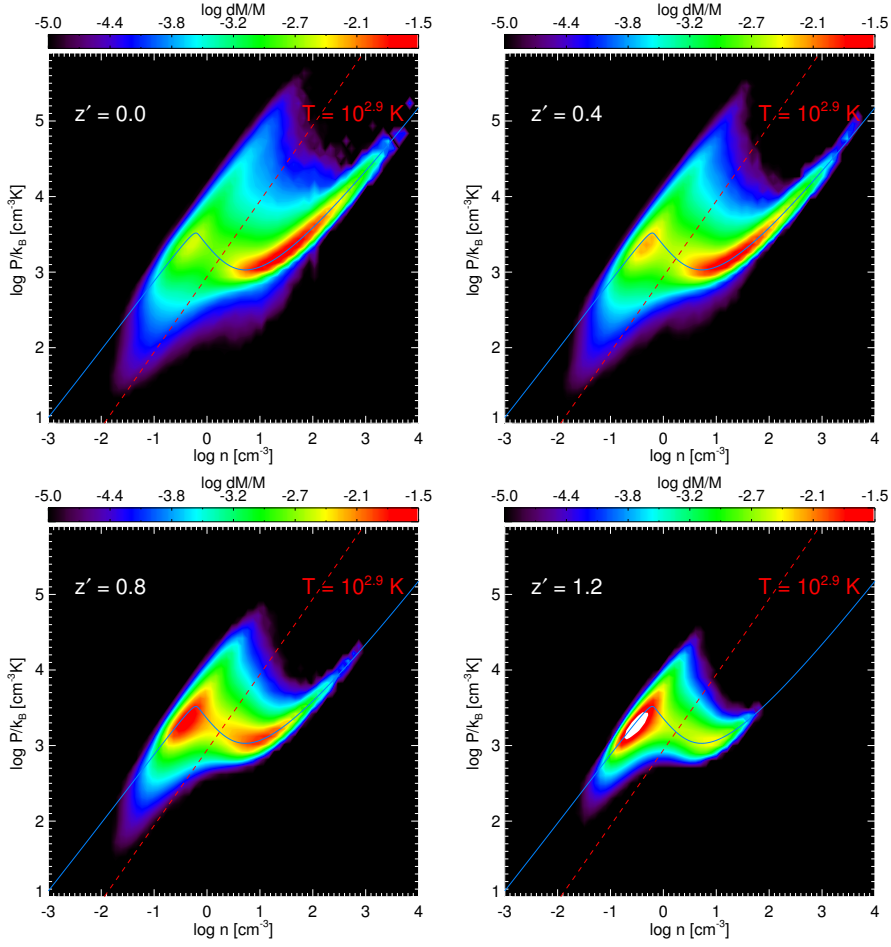


Figure 3.2 Time-averaged mass fractions of the model QA10 on the phase space of density and pressure plane of gas at different vertical distances, $z' = 0.0, 0.4, 0.8,$ and 1.2 , where z' is the normalized vertical distance with the scale, H_n . The solid blue line is the locus of thermal equilibrium with $\langle \Gamma \rangle = 0.61\Gamma_0$, and the dashed red line denotes $T = 10^{2.9}$ K in each panel. The color bar in each panel represents the logarithm of mass-fraction at each logarithm density bin. Most of the gas at z' are in a cold phase. However, as the vertical distance increases, the mass fraction of warm gas increases.

3.2.2 Analysis Methods

We calculate mass-weighted PDFs of volume and column densities in a thin slab around z' . We focus on the mass distributions of the ISM, since the hot gas component, which is missed in the current numerical models, would have a negligible mass fraction but a significant volume fraction. We show the mass distribution of the warm gas component only to clarify its contribution to the mass-weighted dPDF. We define the normalized volume density $s \equiv \log(n/\langle n \rangle_{z'})$, the normalized column density $S \equiv \log(N/\langle N \rangle_{z'})$, the normalized volume density of the warm phase component $w \equiv \log(n_{\text{warm}}/\langle n_{\text{warm}} \rangle_{z'})$, and the normalized volume density of the cold phase component $c \equiv \log(n_{\text{cold}}/\langle n_{\text{cold}} \rangle_{z'})$, where the column density N is the summation along the \hat{y} -direction, n_{warm} is the number density of the warm medium defined by the gas with temperature above a certain temperature range, n_{cold} is the number density of the cold medium ($T_{\text{cold}} \simeq 50 - 100$ K and $T_{\text{warm}} \simeq 6000 - 10000$ K, see Ferriere (2001)[13]), and $\langle \dots \rangle_{z'}$ denotes the horizontal average at z' . At a given time, we first select two thin slabs at a vertical distance of z' in the upper and lower sides with a thickness of 6 parsecs of 3 $x - y$ planes around. We then calculate the mean densities and dPDFs of the slabs at z' , and take a temporal average over more than three t_{osc} in the saturation state ($t_{\text{orb}} > 0.5$) for better statistics.

A two-dimensional PS at each height is calculated to show the variation of the density and velocity structure with the vertical distance. Like 2-D dPDF, a 2-D PS is calculated in the thin slabs at a vertical distance z' . Prior to adopt the 2-D PS tool to the numerical simulations, we restore the periodic boundary condition from galactic rotation by the method of

Hawley et al. (1995)[18]. Then we get power spectra at the three $x - y$ planes in each slab. After we got the 2-D velocity PSs, we split the velocity PSs into the compressible and the solenoidal components by Helmholtz decomposition to show the distribution of compressibility along the vertical direction: $\tilde{v} = \tilde{v}_c + \tilde{v}_s$, where \tilde{v}_s is the solenoidal component of the velocity field and \tilde{v}_c is the compressive component in Fourier space, and they should satisfy the following relations, $\nabla \cdot \tilde{v}_s = 0$ and $\nabla \times \tilde{v}_c = 0$. The 2-D PSs at each height are calculated by the following equations:

$$P_c(k_{2D}) = \frac{1}{N^2} \sum_{i,j} |\tilde{v}_{c,i,j}(k_{2D})|^2, \quad (3.3)$$

$$P_s(k_{2D}) = \frac{1}{N^2} \sum_{i,j} |\tilde{v}_{s,i,j}(k_{2D})|^2, \quad (3.4)$$

where N is the total number of either compressible or solenoidal velocity component, k_{2D} is 2-D wave number, and $\tilde{v}_{c,i,j}(k_{2D})$ and $\tilde{v}_{s,i,j}(k_{2D})$ are Fourier-transformed compressible and solenoidal velocity components, respectively. Finally we take the average of the 2-D density and velocity power spectra over the slabs spatially and temporally at each normalized height, z' .

Federrath et al. (2010)[12] shows the ratio of compressibility in Fourier space:

$$\Psi = \frac{P_{\text{comp}}(k)}{P_{\text{comp}}(k) + P_{\text{sol}}(k)}, \quad (3.5)$$

where P_{comp} and P_{sol} is the Fourier spectra of compressibility and solenoidal components, respectively. They show the compressibility ratio approaches 1/3 in the inertial range where interstellar turbulence is purely driven by solenoidal forcing, whereas the ratio goes higher to 1/2 by purely compressive forcing. Considering this result of Federrath et al. (2010)[12], we expected the time-averaged ratio of compressibility in a thin slab to be

in the range between $1/3 - 1/2$. Now we introduce a new quantity η_{2D}^2 , the ratio of compressibility defined below, which is easy to calculate and visualize the compressibility of a medium in real space. The ratio is calculated in real 2-D plane at each height and each time with the following equation:

$$\eta_{2D}^2 = \frac{|\nabla \cdot v_{2D}|^2}{|\nabla \cdot v_{2D}|^2 + |\nabla \times v_{2D}|^2}. \quad (3.6)$$

For the above equation, we first calculate the divergence and curl of a velocity field in the 2-D $x - y$ plane using, for example, a central difference scheme

$$\begin{aligned} \nabla \cdot v_{2D} \simeq & \frac{v_{x,2D}(i+1, j, k) - v_{x,2D}(i-1, j, k)}{2\Delta x} \\ & + \frac{v_{y,2D}(i, j+1, k) - v_{y,2D}(i, j-1, k)}{2\Delta y}, \end{aligned} \quad (3.7)$$

$$\begin{aligned} \nabla \times v_{2D} \simeq & \frac{v_{y,2D}(i+1, j, k) - v_{y,2D}(i-1, j, k)}{2\Delta x} \\ & - \frac{v_{x,2D}(i, j+1, k) - v_{x,2D}(i, j-1, k)}{2\Delta y}, \end{aligned} \quad (3.8)$$

where v_{2D} is velocity on the $x - y$ plane. When we calculate the above equations at the boundaries, we use a periodic boundary condition.

3.3 Results

3.3.1 Density Probability Distribution Function

Double-peaked density PDF

The density PDFs are varied with height significantly. Fig. 3.3 shows the time-averaged mass fractions of volume (left panel) and column density (right panel) of the fiducial model QA10. In each panel, mass fractions are plotted with 10 solid lines following the rainbow color table from the midplane (red, $z' = 0$) to higher z' (purple, $z' = 1.8$) with $\Delta z' = 0.2$ interval. In the left panel for volume density PDFs, we could see wide and double-peaked dPDFs in low z' , which is shown in the results of Gazol and Kim (2013)[11], where they show the doubled-peaked volume density PDFs for the bistable turbulent flows with increasing Mach numbers.

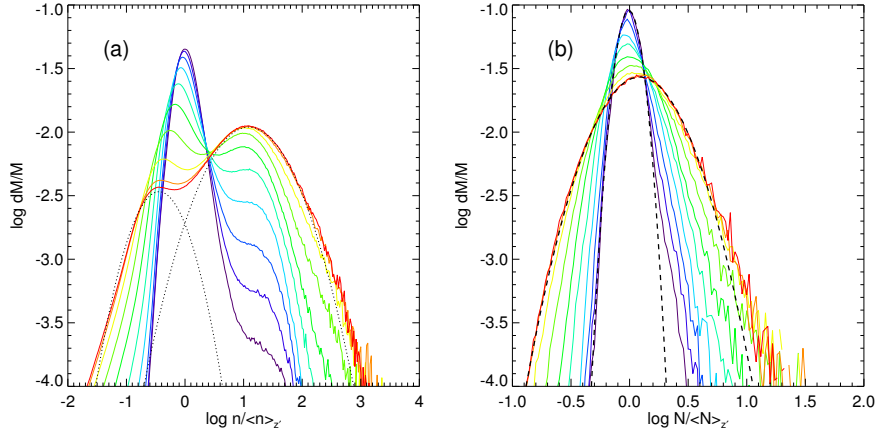


Figure 3.3 Time-averaged mass fractions of (a) volume density and (b) column density of the fiducial model normalized by their averages at each height in logarithmic scale. The lines with different colors in both panels show mass fractions at various heights from the midplane, $z' = 0.0$ to $z' = 1.8$, which correspond to the rainbow color table from red to purple, respectively. The dotted lines in the left panel are Gaussian fits for the warm and cold media at $z' = 0.0$. The two dashed lines are Gaussian fits for the column density PDFs at $z' = 0.0$ and $z' = 1.8$. The volume density PDFs near the midplane show double-peaked shape, but the volume density PDFs at upper hemisphere approach a lognormal distribution.

The high-density peak ($s > 0$) is dominant near the midplane and falls with increasing height, whereas the left peak in the low-density region becomes dominant toward higher z' and its position moves to the higher density region. This is just because the mass fractions between cold and warm are changed with z' . The right panel of Fig. 3.3 shows the overall column density PDFs to be positively skewed Gaussian distribution compared with the dashed Gaussian fitted lines. The dispersions of the column density PDFs are almost half of those of volume density (notice the range of the horizontal axis). When 3-D density cubes are integrated along either x or y directions, the density contrast would be smoothed out. So the dispersions of column density PDFs will be decreased. The column density PDF seems to have a power-law tail to the high-density region. But the deviation of a power-law tail from LN distribution is not quite significant compared to the high-density peak of volume density PDFs in the left panel.

To identify the individual components of the double-peaked shape of the mass-weighted PDFs of volume density, we separated the gas into warm (red line) and cold (blue line) phases and made density PDFs for each phase in Fig. 3.4. We have seen the separation of the gas in phase diagrams of, for example, Fig. 3.2 into the warm and cold phases with a certain temperature. In order to determine such a temperature for each numerical model, we investigated the time-averaged and mass-weighted temperature PDF of each model and found a local minimum temperature, which is taken as a phase transition temperature, T_{pt} which separates the gas into the warm and cold phases. The phase transition temperatures of the numerical models, QA02, QA05, QA10, QA20, are $10^{2.45}$, $10^{2.6}$, $10^{2.9}$, $10^{3.1}$ K, respectively. To make a comparison of the den-

sity PDFs at lower and higher heights, we selected two horizontal layers. The left panels of Fig. 3.4 show density PDFs near the galactic midplane over the heights of $0.0 \leq z' \leq 0.2$ and the right panels show density PDFs at higher- z' , $1.0 \leq z' \leq 1.2$. From top to bottom, density PDFs of numerical models are ordered with the increasing model number.

We can clearly see a double-peaked shape of density PDFs of the total gas for not only the fiducial model, QA10, but also other models in Fig. 3.4 and the origin of the double-peaked shape is due to the two-phase nature of the gas. The difference among the density PDFs of models is the relative heights of the two peaks. Toward the bottom row, the right peak becomes higher than the left one. The reason is that the cooling and self-gravity in the QA20 model with the highest surface density are more efficient than the one in other models, which builds the right peak at the high-density region in low- z' . In the right panels of the high- z' , the warm phase is dominant, and the mass fractions of the cold phase are quite different among models. The mass fraction of the cold phase is slightly smaller than that of the warm medium in the (h) panel, whereas the mass fraction of the cold phase is negligible in the (b) panel.

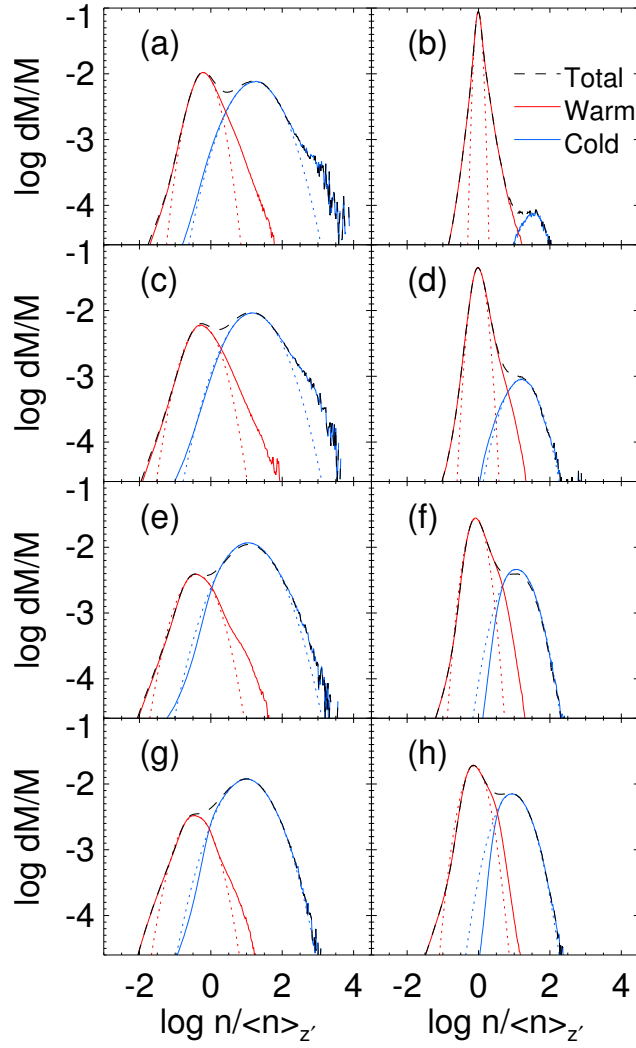


Figure 3.4 Time-averaged mass fractions of density PDFs for four different numerical models. In each panel, the red and solid blue lines are the mass fractions of PDFs for the warm and the cold gas components, respectively. The black dashed line is for the combined warm and cold gas components. Each density PDF is averaged over $0.0 < z' \leq 0.2$ near the midplane shown in the left panels and $1.0 < z' \leq 1.2$ at the higher z' in the right panels of the four numerical models, QA02 (a, b), QA05 (c, d), QA10 (e, f) and QA20 (g,h). The dotted lines are Gaussian fits for the warm and the cold gas.

Mean, dispersion, and skewness of dPDF with height

We calculated mass-weighted mean (μ), dispersion (σ^2), and skewness (γ) for four different normalized densities; volume density (s), column density (S), the density of the warm medium (w), and the density of the cold medium (c), described in the previous section. The equations for the mass-weighted statistics of the densities are as follows:

$$\mu_q = \frac{\int q dM}{\int dM}, \quad (3.9)$$

$$\sigma_q^2 = \frac{\int (q - \mu_q)^2 dM}{\int dM}, \quad (3.10)$$

$$\gamma_q = \frac{\int ((q - \mu_q)/\sigma_q)^3 dM}{\int dM} \quad (3.11)$$

where q represents the four normalized densities. Fig. 3.5 provides time-averaged mass-weighted mean (the left column), dispersion (middle), and skewness (the right) of normalized density with height for the four numerical models. Those statistics are plotted for volume density (upper panels, (a)~(c)), and column density (middle, (d)~(f)), and the density of warm phase (bottom, (g)~(i)). In each plot, the colors of the solid lines denote the statistics of numerical models of QA02 (red), QA05 (green), QA10 (blue), and QA20 (black). We could see that mean and dispersion become smaller with increasing height, and that skewness is roughly positive or close to zero.

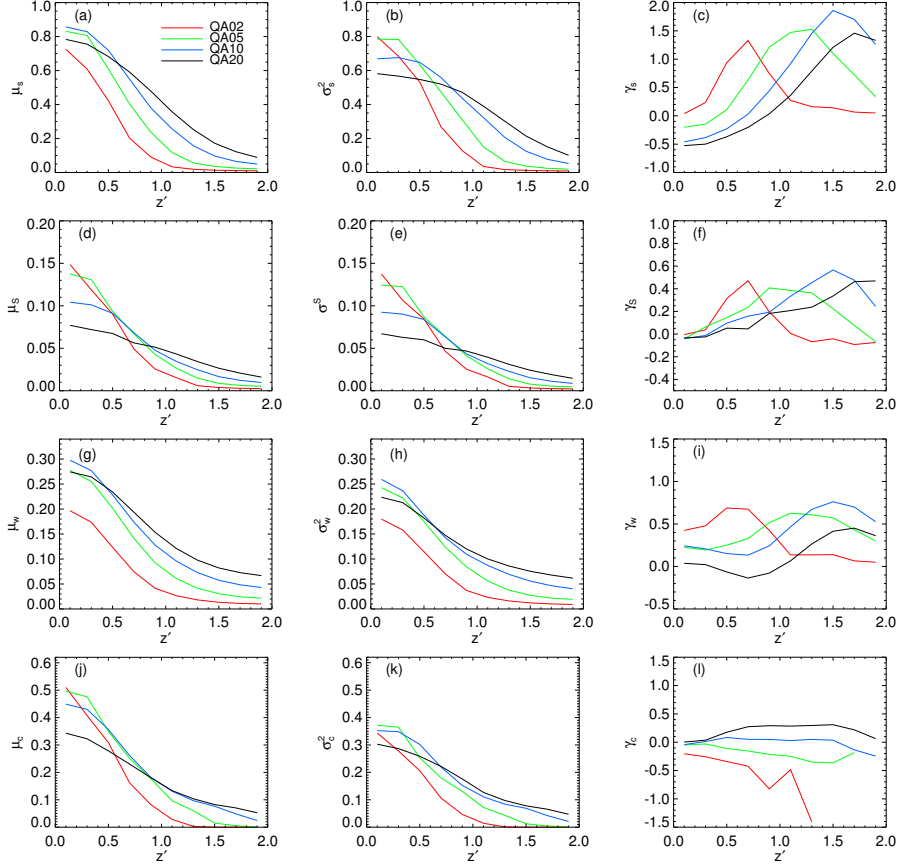


Figure 3.5 Time-averaged means (left), dispersions (middle), and skewnesses (right column) of the density of the four numerical models with height. The statistics for the total volume density (top), the column density (the 2nd row), the density of the warm gas (the 3rd row), and that of the cold gas (bottom) are plotted. Each color of the line denotes the four models: QA02(red), QA05(green), QA10(blue), and QA20(black).

The mass-weighted mean of normalized density significantly deviates from zero at the lower height. Two competitive reasons could explain the deviation. First, as shown in Fig. 3.5, cold phase has a larger mass fraction in the model with denser surface density, which pulls the mean of the total volume density to the denser region of density PDF. At low- z' , Fig. 3.5(a) shows the means of three models, QA02, QA05, and QA10, are mostly affected by the cold phase fraction. At high- z' , the means are proportional to not only the surface density but also the gas fraction blown off by the SN explosions. The average of the model QA20 in low- z' shown in Fig. 3.5(a) is smaller than those of QA05 and QA10 models. It is because of the violent SN explosions. It is also the same reason that the mean of the column density near the midplane of the model QA20 in the panel (d) is smaller than the other models. The dispersions as a function of the height in the panels of (b), (e), (h) and (k) show a similar trend as the means in the panels. So distributions of the mean and the dispersion with height could be explained by the competition of the fraction of cold phase and SN explosions.

As can be seen from panels (c) and (f), the skewnesses of the volume and the column densities as a function of height show a quite similar trend to each other. The skewness grows up to at a certain height and then decreases. We could explain this behavior with a comparison between the mass fractions of warm and cold phases. Near the midplane, the mass fraction of cold phase is comparable to or larger than that of the warm phase, which provides almost zero skewness or negative skewness, respectively. With increasing height, the skewness grows until the cold medium is negligible as we have seen in Fig. 3.4 and Fig. 3.5. Since the temperature is increasing with height, the medium becomes rarefied to

make the dPDF at the low-density region rising for skewness to decrease to 0 again.

In panels of (g) and (h), means and dispersions of the warm phase are larger with higher model number except for the model QA20. The most of the warm gas in upper height is in an almost isothermal state shown in Fig. 3.2. If we concentrate a horizontal upper layer, then there is no vertical stratification of gas distribution in the layer. Furthermore, the gas mass contained in the layer is almost constant in a statistical sense. It is a well known through numerical simulations that an LN distribution describes well the density PDF of the isothermal turbulence and there is a unique relation between the mean and dispersion of the LN density PDF if the total mass of a system is conserved. We expect that there will be a correlation between the mean and the dispersion of warm gas in a horizontal layer at a particular height in our models. In fact, the bottom panels of (g) and (h) show a clear relationship between means and dispersions of the warm phase. Detailed description for rms sonic Mach number with height and the relationship between statistics and Mach number will be explained in the discussion section. The skewnesses of the warm medium in the panel (i) are very similar to the other panels of skewness except for the behavior at low- z' . The skewness fluctuates around 0 following blue (QA10) and black (QA20) lines, which is because the phase separation by temperature criterion could not be a proper method so that the cold medium might be overlapped in the warm medium each other.

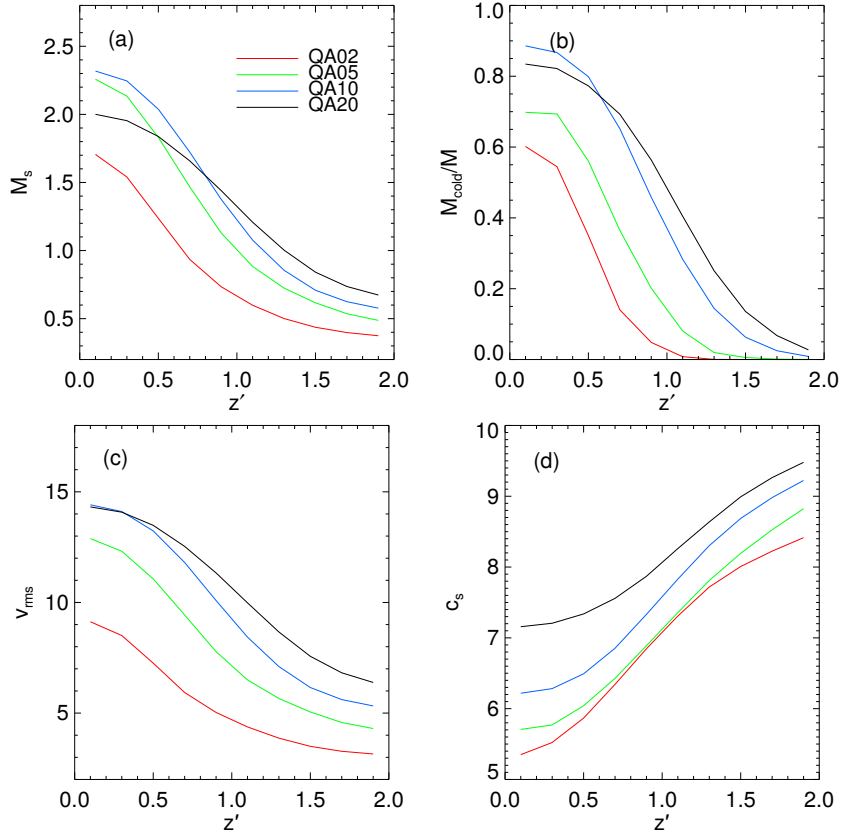


Figure 3.6 Rms sonic Mach number (a), the mass fraction of cold phase gas (b), rms velocity (c), and sound speed as a function of z' . The colors of the lines are the same to those of the previous figure with the four models.

The Mach number distribution at the upper left panel in Fig. 3.6 is very similar to those of the mean and the dispersion of warm phase in the panels (g) and (h) of Fig. 3.5. Gradual decrease of Mach number with increasing height could be explained by the vertical distribution of the sound speed, $\langle c_s \rangle_{z'}$ in the panel (d), and the rms velocity, $\langle v_{rms} \rangle_{z'}$ in the panel (c), where the time averaged and volume-weighted rms sonic Mach number with height is defined as, $M_s(z') \equiv \langle \langle v_{rms} \rangle_{z'} / \langle c_s \rangle_{z'} \rangle_t$. The vertical distribution of the sound speed follows that of temperature, where the average temperature is $\sim 10^2$ K in low- z' and $\sim 10^4$ K in higher- z' , whereas rms velocity becomes faster toward the midplane due to the violent SN activity there. The QA20 model has a lower Mach number distribution near the midplane than those of QA10 and QA05. Since the rms velocity of the gas is saturated near the galactic plane in the panel (c) whereas the sound speed increases with higher model numbers systematically, this reverse could happen. Moreover, for the model QA20, the gas in cold phase has blown off by strong SN activity near the midplane. The mass fraction of cold gas is relatively lower compared to those of QA05 and QA10 models near $z' = 0$ in the panel (b). Then the gas is heated up to become warm. As a result, the distribution of the sound speed near the midplane becomes relatively high and makes the Mach number distribution there become lower than those of the other two models.

3.3.2 Power Spectra of Density and Velocity

Fig. 3.7 presents power spectra of volume density and velocity of horizontal layers at different heights of the fiducial model, QA10. In Fourier space, a velocity field could be separated into compressive and solenoidal components by Helmholtz decomposition. Their power spectra are also shown in the lower two panels of Fig. 3.7. In each panel, a rainbow color table is used for describing the PS with different heights from low (red) to high- z' (purple) like Fig. fig34. Because of relatively poor numerical resolution of our models, there is not enough inertial range to determine the correct power index of each spectrum. However, we plotted slopes of Kolmogorov and Burgers spectra with dotted lines for comparison purpose in each panel, where Kolmogorov's spectrum has power index of $-5/3$ and Burgers of -2 in 2-D space. The vertical dashed lines denote the initial radius of SNR of 10 pc set by K13. Interestingly, below the radius scale, the power decreases quite rapidly.

As can be seen in the panel (a), the density power spectrum becomes steeper with height. Following the red line near the galactic midplane, the PS is much shallower than Kolmogorov's. But in higher z' , PS becomes steeper and approaches $-5/3$. We could explain the variation of the power index with the results of Kim and Ryu (2005)[15]; the density PS flattens as the rms Mach number of a system rises. The rms Mach number could be expected to become smaller with increasing height since the sound speed goes higher due to the temperature distribution in the vertical direction whereas the rms velocity becomes faster toward the midplane due to SN explosions. So, this result is consistent with that of Kim and Ryu (2005)[15].

The power spectrum of velocity, on the contrary, flattens with increasing height as seen in panels of (b), (c), and (d). The relationship between the power index and rms Mach number in Gazol and Kim (2010)[10] shows that the velocity PS steepens when the rms Mach number increases. The power slope of PS is close to $-5/3$ in the high- z' approximately, but it is close to or steeper than -2 near the midplane in the panel (b). What is interesting for this result is that the index looks greater than that of Burgers spectrum from shock-dominated turbulence. We might find the reason from the power spectrum of the compressive velocity component in the panel (c). Since the forcing of turbulence is totally from the physical source of SN explosions, the gas nearby SN explosions must be compressed highly. And that leads compressive component to become dominant in power distribution on large scales around the SNR size compared to the solenoidal one shown in the panel (d). But, since solenoidal PS is shallower than $-5/3$, the power of solenoidal component is nearly equal or higher than that of compressive one on small scales at around 10 pc scale. In summary, these results suggest that the highly compressive component on large scales would be converted into the solenoidal component with increasing wave number and finally the solenoidal component would survive on small scales. Because of poor numerical resolution, these results should be confirmed with higher resolution simulations.

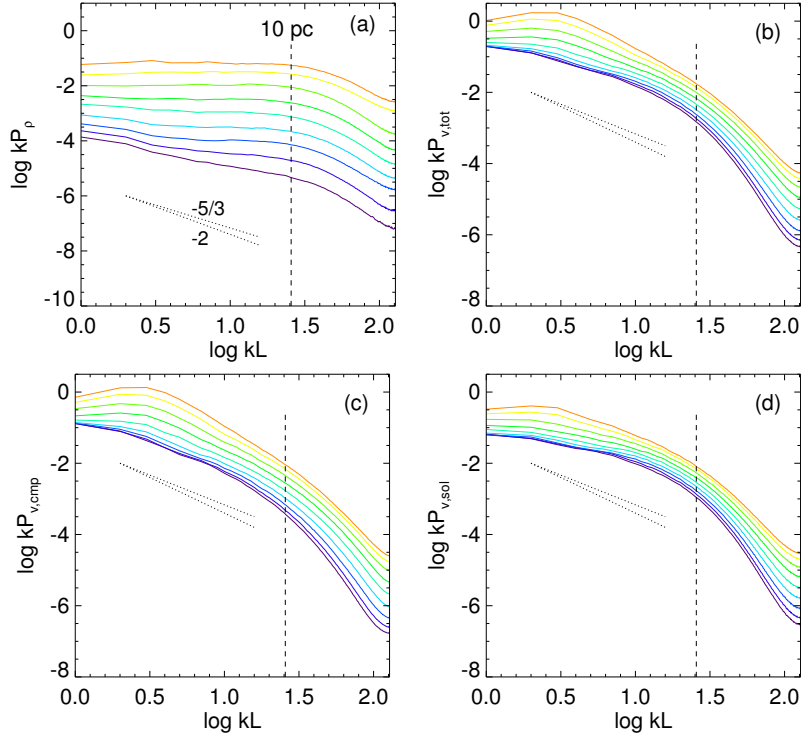


Figure 3.7 Time-averaged power spectra of (a) density and (b) velocity field, and (c) compressive component and (d) solenoidal components of the velocity field of model QA10. Like Figure 3.3, the colors denote spectra at different heights. A dashed line in each panel shows a 10 pc scale of the initial radius of a supernova remnant, and dotted lines show the slopes of $-8/3$ and $-11/3$ for comparison purpose.

3.3.3 Measurement of the Compressibility in Real Space

Fig. 3.8 (a) shows a snap of the compressibility defined in equation (3.6) in the whole computational box. The left panel (b) shows the compressibility as a function of the vertical height from the midplane. We first calculated the squares of divergence of velocity for the compressible component and curl of velocity for the solenoidal component in 2-D real space at each height and then take the ratio in equation (3.6), which is, in fact, a good measure of compressibility. This is a new method which easily enables us to get characteristics of compressibility without resort to Fourier transform in Federrath et al. (2010)[12]. The compressibility ratio is visualized directly in real space in the panel (a) where the snapshot is drawn at $t \sim t_{orb}$ and the compressibility is color-coded with the rainbow color table. The distribution of η^2 is quite complicated. One striking feature of the η^2 distribution is several bubbles shown in red color, which corresponds to a maximum η^2 value. The newly born SNRs develop the bubbles at low- z' . The bubbles should have very high η^2 values due to compressive motions of shock propagation along a radial direction from each SN explosion. The η^2 distribution looks very clumpy following the distribution of SNRs and shocks around them, and the contrast of η^2 looks large between the regions with and without an SNR.

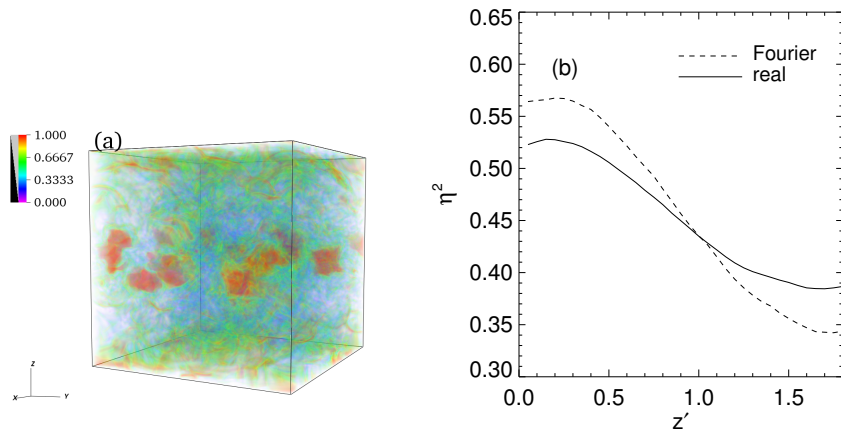


Figure 3.8 A snapshot for the ratio of compressibility in a three-dimensional cube at $t/t_{orb} \sim 1$ of our fiducial model, QA10 (a) and time-averaged compressibility ratio with height (b). Several SNRs are seen in red near the midplane in the left panel. The dashed line in the right panel denotes the ratio measured in Fourier space, and the solid line shows the ratio in real space.

We averaged the ratio of compressibility over the 2-D plane in a thin slab at each height and time, measured both in real space and Fourier space with solid and dashed lines in the panel (b), respectively. Both lines vary between the lines of $\beta = 0.35$ and 0.55 and depend on height. Federrath et al. (2010)[12] show compressibility in Fourier space, which ranges between $1/3 \sim 1/2$ for dominant solenoidal component and dominant compressive component, respectively. So the compressibility near the midplane would become about $1/2$ by the strong SN explosions, and it approaches $1/3$ to higher- z' since there is little influence of SNRs. Our results show slightly larger values compared to the results of Federrath et al. (2010)[12], which might arise from the artificial compression due to the global oscillation described in Fig. 3.2.

From the sliced images shown in Fig. 3.9, we can see that the propagation of SN shocks generates quite high compressive and solenoidal components. We sliced the computational cube at 32 pc from the midplane and showed the compressibility, η^2 , in the panel (a) of Fig. 3.8, as an image with the rainbow color table shown in the panel (a). The high compressibility regions correspond to newly born SNRs, and filamentary structures follow shocks nearby the SNRs. We calculated the squares of divergence and curl of the velocity field in the white rectangular region, where a newly-born SNR resides and made images of them in the panels of (b) and (c). The compressive component shown in the (b) panel is dominant, especially, inside an SNR and around its shock front. On the contrary, we can see there are many filamentary structures around the SNR shock in solenoidal velocity component in the panel (c). The panel (d) shows both the compressive and the solenoidal component to show the positional difference of both components clearly. We put the contour

lines for the solenoidal velocity component on the background image of the compressive velocity component shown in the panel (d). The solenoidal component might appear where the curved shock is bent and broken by unstable fingers of SNRs in later stages or by the pre-existing clumpy and dense structures around. These results show that even in highly compressive velocity component driven by SNe, the solenoidal velocity component could be generated near the highly compressive curved shocks.

We measured the relationship between time-averaged rms sonic Mach number, M_s , and velocity compressibility, η^2 , at each height of the models with different colors shown in (a) of Fig. 3.10. The colors of the solid lines are the same to those of Fig. 3.11. The dashed lines represent the results of linear fittings for the solid lines. The velocity compressibility of models calculated in real space as a function of the vertical distance is shown in the panel (b). The time-averaged rms sonic Mach number, $\langle M_s \rangle_t = \langle \langle v_{rms} \rangle_{z'} / \langle c_s \rangle_{z'} \rangle_t$, at each height is plotted in panel (c).

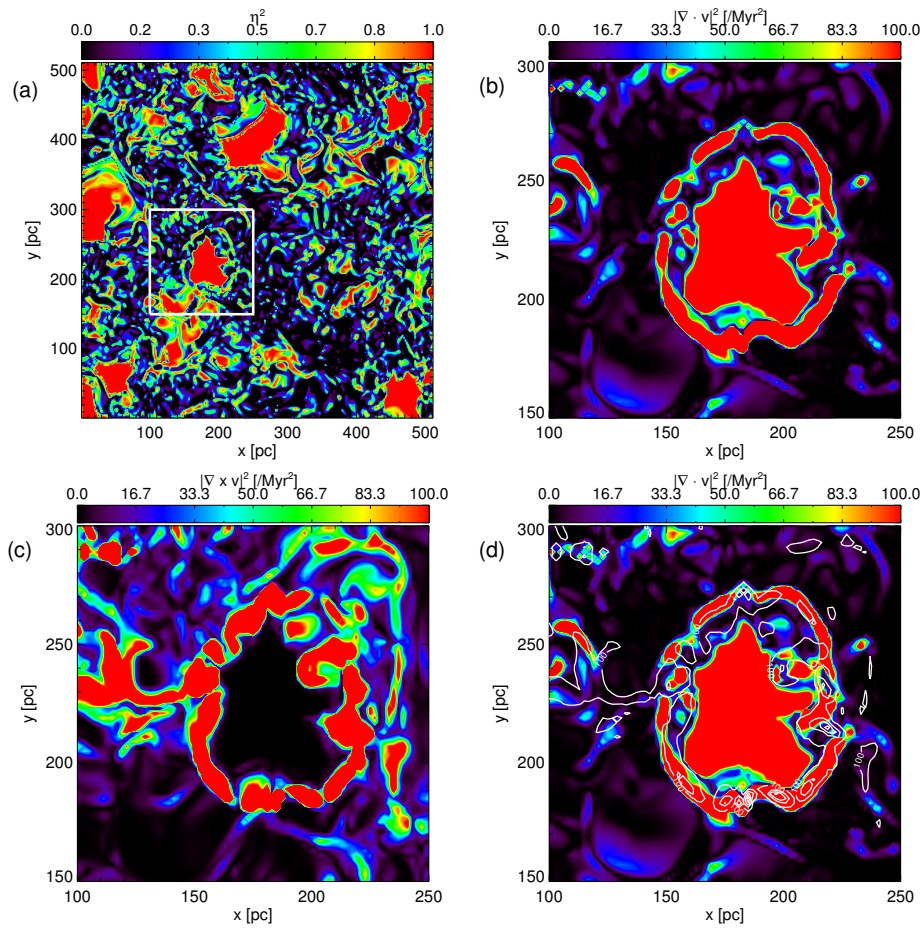


Figure 3.9 The sliced image (a) of at $z' = 32$ pc of the compressibility of a computational cube shown in Figure 3.8, and the magnified slices of divergence of velocity (b) and curl of the velocity (c) around an SNR. The panel (d) shows a comparison of compressive and solenoidal velocity components, where the solenoidal component is shown in white solid contour lines over the image of the compressive component. The solenoidal velocity component seems to be generated at the spots where the curved shock is broken.

Fig. 3.10 (a) shows that the Mach number distribution is nearly proportional to that of velocity compressibility measured in real space. The slopes of the lines are very similar to each other. And since SN activity increases as the model number increases, the compressibility also increases systematically. When we make linear fittings of the solid lines, the relations near the boundary and the galactic midplane are ignored. In the panel (b), the compressibility at the ignored heights tends to increase with increasing height in the blue and the black lines for the models of QA10 and QA20, respectively. As we already have seen the divergence and curl of the velocity field in Fig. 3.9, both the compressive and the solenoidal components grow at the same time near the SN explosions. Moreover, violent SN explosions at the midplane could make more curved shocks from interference between SNRs so that the velocity compressibility could be lowered at the midplane.

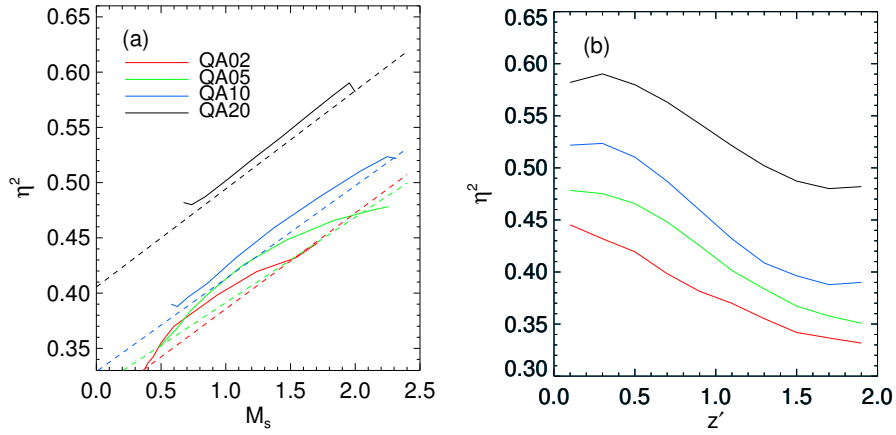


Figure 3.10 The relationship (a) between rms sonic Mach number, M_s , and velocity compressibility, η^2 , for different models. Solid lines are from numerical models, and the dashed lines are the linear fittings of solid lines. The colors of solid lines correspond to the models shown in (a). Velocity compressibility is roughly proportional to M_s . Panel (b) and (c) show the distributions of velocity compressibility and Mach number as a function of vertical distance.

3.4 Discussion

3.4.1 Relation between the Mass-weighted Mean and Dispersion of Density

Previous literature has noted that an LN distribution can describe the density PDF of an isothermal mass-conserving turbulent system and, as a result, there is a unique relation between the mean and the dispersion of density. The relation can be written as $\mu_M = \frac{\ln 10}{2} \sigma_M^2$, (e.g., Ostriker et al. 2001[26]). In the current study, Fig. 3.11 presents the relations between the mean and the dispersion of (a) volume density, (b) volume density with only the warm gas phase and (c) the column density at each height from our results described in result section 3.3.2. The colors of the solid lines in each panel are related to the model numbers as shown in Fig. 3.5 and the dashed line denotes the relation obtained from the LN distribution.

As shown in the panel (a), the relation between mean and dispersion of each model deviates from the relation of Ostriker et al. (2001)[26], since the current numerical simulations are not perfectly satisfied the isothermal mass-conserving requirement of the simple relationship. However, the relationship only for the warm phase shown in (b) is more close to the that of isothermal turbulence. Possible explanations for the similar relation between the two cases are that the warm gas in each horizontal layer (1) is stratified no more in a thin slab (2) is in a nearly isothermal state due to picking up a warm phase gas component only, and (3) almost conserves its mass on the layer in a statistical sense. The nearly isothermal nature of the warm gas in an upper horizontal layer was shown in Fig. 3.11. In the panel (c), the relation in the column density almost sticks to that of the isothermal turbulence case due to fewer fluctuations in col-

umn density than volume density. These findings suggest that we could apply the simple relation between the mean and the dispersion of density for an isothermal turbulence in a mass-conserving system to the realistic turbulence when we confine to the gas that satisfies the requirements for the simple relation.

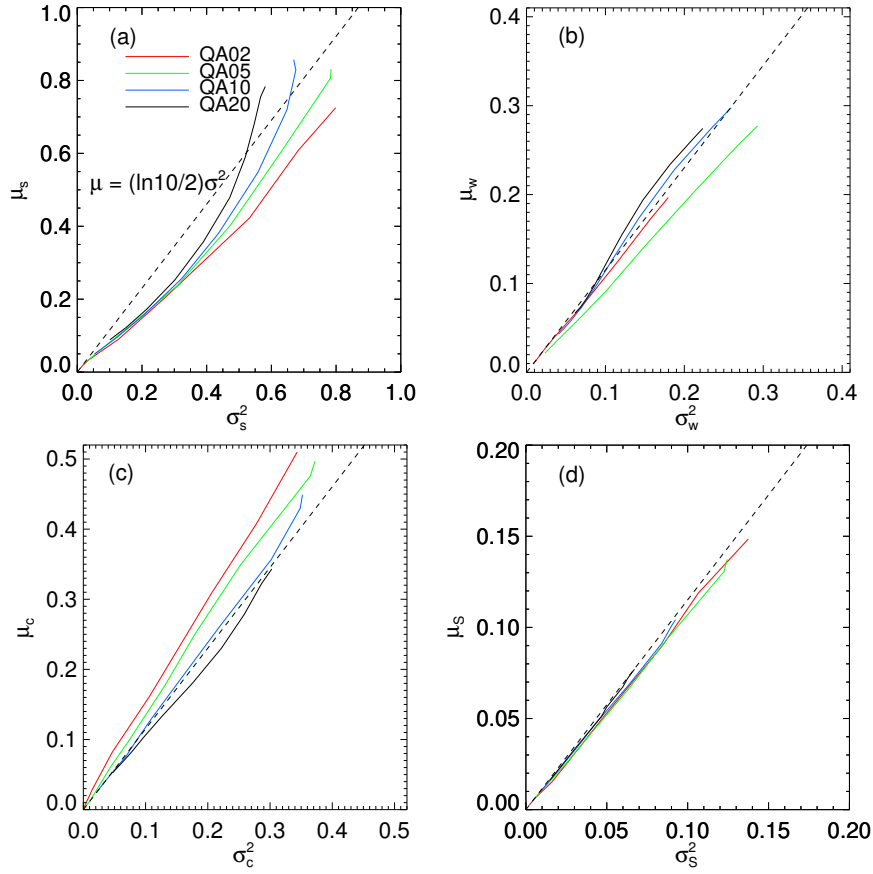


Figure 3.11 Relations between the time-averaged mean and dispersion of the volume density (a), the volume density with only the warm gas phase (b), that with only the cold gas phase (c) and the column density (d). The colors of solid lines represent the relations for different models shown in the panel (a). A dashed line in each panel is the relationship obtained from the log-normal density PDF distribution of an isothermal turbulent flow in a mass-conserving system.

3.4.2 Relationship between RMS Sonic Mach Number and Statistics

Fig. 3.12 provides the relationships of the total volume density (a), the density of the warm gas (b), and the column density (c). In the previous studies, the relationship between Mach number and the dispersion of the density from isothermal turbulence simulations is shown in equation (1). This relationship is plotted in each panel with dashed lines of $b = 0.3, 0.5$ and 1.0 for comparison. Federrath et al. (2008)[8] set b to be 1 when purely compressive forcing perturbs the ISM, $1/3$ when solenoidal forcing and $1/2$ when naturally mixed forcing. Burkhart and Lazarian (2012)[6] applied the relationship to the column density with another multiplying constant, A . They set the constant A to be $1/2$, roughly.

The relationship between Mach number and mass-weighted dispersions of total volume density in the panel (a) seems to be far higher compared to that of dashed line of $b = 1.0$. This is due to the existence of both cold and warm phases, which gives a much broader dispersion of density. From subsonic to transonic, the relationships of the models are very close to each other, but in the supersonic region, which means in lower- z' , they are quite different with each other. Since the density dispersions of models are inversely proportional to the surface density in low- z' shown in Fig. 3.5, the red line of the model QA02 is the highest, and the other lines get lower with increasing model number. However, in the panel (b), the relationship for warm phase of each model is very close to each other, since the warm phase could be thought to be roughly an isothermal state as we consider in the previous section with Fig. 3.11. And the solid lines are in between the lines of $b = 0.5$ and 1.0 , where the gas is highly compressive. In the panel (c), they seem to stay between $b = 0.5$

and 1.0, too. As described in the panel (a), density dispersions of the models are inversely proportional to the surface density. Since the Mach number coverage is limited only to up 2.5 for our numerical simulations, further research over a wider range of Mach number should be needed for determining the relationships among Mach number, compressibility, and density dispersion.

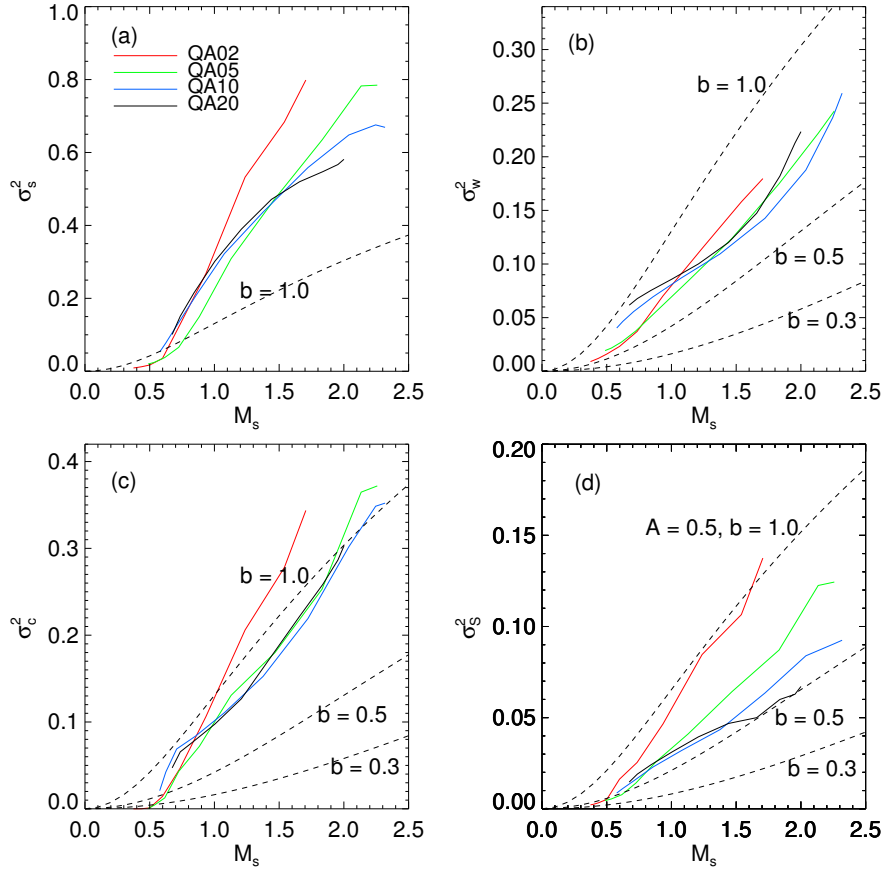


Figure 3.12 The relationship between rms sonic Mach number and dispersions of the total volume density (a), warm gas density (b), cold gas density (c), and column density (d). The solid colored lines represent the relationships for different numerical models indicated in (a). The dashed lines represent the relationship known from turbulent isothermal simulations. b is a constant related to the compressibility of forcing and A is a multiplication constant used for column density (see the main text).

3.5 Summary

We analyzed the statistics of the numerical simulations for the turbulent and stratified ISM from K13 to study density and velocity fields as a function of the vertical distance from the midplane. First, the density probability distribution functions (dPDFs) are varied with height, where the dPDFs have a double-peaked shape at lower hemisphere while the dPDFs in upper hemisphere follow the lognormal distribution. The double-peaked shape was separated into two components contributed from warm and cold gas phases. To quantify the shape of dPDFs, we measured the skewness, and we found that it varied concerning the mass fractions of the warm and cold phases at a given height. We also investigated the means and the dispersions of the density PDFs of the models with height and the relationships between them. The means and the dispersions of the total volume density seem to deviate from the well-known relationship obtained isothermal turbulence simulations described in the previous literature (Ostriker et al. 2001[26]). But for the density PDFs of the warm phase and the column density, the relationships from our numerical models are very close to the previous relationship. Moreover, the rms sonic Mach number and the density dispersions of the volume density of the warm phase and the column density are also shown to be tightly related to each other. There are limitations to expand our results to the general studies for interstellar turbulence. For instance, the models we have chosen do not deal with a hot component of the ISM. To make up this weak points, we only measured the mass fractions of the density PDFs since the hot component would have huge volume fraction but a low mass fraction. So in a mass fraction, interpretation in the results could be expanded.

We, secondly, measured the power spectra (PS) of density and velocity with height. The density PS becomes steeper with increasing height while the velocity PS shallower. We could separate the velocity field into compressive and solenoidal components and found that the power of the solenoidal component decreases more slowly with decreasing scale. Thirdly, a new method was proposed to measure easily velocity compressibility in real space (see eq. 3.6). The velocity compressibility was shown to have in between the lines of $\eta^2 = 0.35$ and 0.55 . This range of the velocity compressibility is comparable to that measured in Fourier space. In a 3-D real cube and on a sliced horizontal plane, we visualized the velocity compressibility and verified that an SN explosion could be a source for generating the strong compressive velocity component. At the same time, the solenoidal velocity component is shown to be caused by the curved shock near the SNR. We found well-defined linear correlations between the rms sonic Mach number and velocity compressibility for our numerical models. The slopes of the relationships have a similar value of $1/11$ for all our models. Also since the range of Mach number is set around a transonic region, the statistics such as dispersions of density, compressibility ratio should be researched over wider Mach number range. And the energy source could be magnetorotational instability in the environment of lower SN activity and comparable to that of SN explosions. In there, we should consider the galactic shear motion and magnetic field together. In future work, we could adopt the same statistical methods dealt in the current study to the models including more realistic physical ingredients such as magnetic fields and hot medium.

Bibliography

- [1] Agertz, O., Lake, G., Teyssier, R., Moore, B. Mayer L. & Alessandro B. R. 2009, MNRAS, 392, 294
- [2] Armstrong, J. W., Rickett, B. J., & Spangler, S. R. 1995, ApJ, 443, 209
- [3] Avillez, M. 2000, MNRAS, 315, 479
- [4] Balsara, D., Benjamin, R. A., & Cox, D. P. 2001, ApJ, 563, 800
- [5] Bonazzola, S., Heyvaerts, J., Falgarone, E., Perault, M., & Puget, J. L., 1987, A&A, 172,293
- [6] Burkhart B., & Lazarian, A., 2012, ApJL, 755: L19
- [7] Chepurnov, A., & Lazarian, A. 2010, ApJ, 710, 853
- [8] Cho, W., & Kim, J., 2011, MNRAS, 410, 8
- [9] Dib, S., & Burkert, A., 2005, ApJ,630, 238
- [10] Elmegreen, B. G., & Scalo, J. 2004, ARA&A, 42, 211
- [11] Federrath, C., Klessen, R. S., & Schmidt, W. 2008, ApJ, 688, 79

- [12] Federrath, C., Roman-Duval, J., Klessen, R. S., Schmidt, W. & Mac Low, M.- M., 2010, *A&A*, 512, 81
- [13] Ferriere, K. M., 2001, *RvMP*, 73, 1031
- [14] Gazol, A. & Kim, J., 2010, *ApJ*, 630, 911
- [15] Gazol, A. & Kim, J., 2013, *ApJ*, 765, 49
- [16] Gent, F. A., Shukurov, A., Sarson, G. R., Fletcher, A., & Mantere, M. J. 2013, *MNRAS*, 435, 689
- [17] Hall, A. N., 1980, *MNRAS*, 190, 353
- [18] Hawley, J. F., Gammie, C. F., & Balbus, S. A. 1995, *ApJ*, 440, 742
- [19] Joung, M. K. R., & Mac Low, M.- M., 2006, *ApJ*, 653, 1266
- [20] Kim, J., & Ryu, D. 2005, *ApJ*, 630, L45
- [21] Kim, C-G., Ostriker, E. C., & Kim, W-T 2013, *ApJ*, 776, 1
- [22] Kim, C-G., Ostriker, E. C., & Kim, W-T 2014, *ApJ*, 786, 64
- [23] Kim, C-G., & Ostriker, E. C., 2015, *ApJ*, 815, 67
- [24] Klessen, R. S., 2000, *ApJ*, 535, 869
- [25] Kolmogorov, A. 1941, *DoSSR*, 30, 301
- [26] Kritsuk, A. G., Usyugov S. D., & Norman, M. L., 2011, *IAUS*, 270, 179
- [27] Larson, R. B. 2003, *RPPh*, 66, 1651
- [28] Li, P. S., Norman, M. L., & Mac Low M.- M., & Heitsch, F., 2004, *ApJ*, 605, 800

- [29] Mac Low, M.- M., & Klessen, R. S., 2004, *RvMP*, 76, 125
- [30] Molina, F. Z., Glover, S. C. O., Federrath, C., & Klessen, R. S., 2012, *MNRAS*, 423, 2680
- [31] Nordlund, A., & Padoan, P., 1999, In *Interstellar Turbulence, Proc., 2nd Guillermo Haro Conf.*, ed., J, Franco, A., Carraminana, pp., 218, Cambridge: Cambridge Univ. Press
- [32] Ostriker, E. C., Gammie, C. F., & Stone, J. M., 1999, *ApJ*, 513, 259
- [33] Ostriker, E. C., Stone, J. M., & Gammie C. F. 2001, *ApJ*, 546, 980
- [34] Padoan, P., Jones, B. J. T., & Nordlund, A. P. 1997, *ApJ*, 474, 730
- [35] Passot, T., & Vázquez-Semadeni, E. 1998, *Phys. Rev. E*, 58, 4501
- [36] Price, D., Federrath, C., & Brunt, C. 2011, *ApJ*, 727, 21
- [37] Scalo, J., Vázquez-Semadeni, E., Chappell, D., & Passot, T., 1998, *ApJ*, 504, 835
- [38] Stone, J. M., Gardiner, T. A., Teuben, P., et al., 2008, *ApJS*, 178, 137
- [39] Stone, J. M., & Gardiner, T. A., 2009, *New Astron.*, 14, 139
- [40] Tasker, E. j., & Bryan G. L., 2006, *ApJ*, 641, 878
- [41] Thorton, K., Gaudlitz, M., Janka, H.-Th., & Steinmetz, M., 1998, *ApJ*, 500, 95
- [42] Vázquez-Semaceni, E., 1994, *ApJ*, 423, 681

- [43] Vázquez-Semadeni, E., Passot, T., & Pouquet, A., 1995, *ApJ*, 441, 702
- [44] Vázquez-Semadeni, E., Ostriker, E. C., Passot, T., Gammie, C. F., & Stone, J. M. 2000, in *Protostars and Planets IV*, ed. V. Mannings, A. P. Boss, & S. S. Russell (Tucson: Univ. Arizona Press), 3
- [45] Vázquez-Semadeni, E., González, R. F., Ballesteros-Paredes J., Gazol, A., & Kim, J., 2008, *MNRAS*, 390, 769
- [46] Wada, K., Meurer, G., & Norman, C. A., 2002, *ApJ*, 577, 197
- [47] Wada, K., & Norman, C. A., 2007, *ApJ*, 660, 276
- [48] Wentzel, D. G., 1968, *ApJ*, 152, 987

Chapter 4

Statistical Properties in the Outer Spiral Arm in the I-GALFA HI 21 cm Line Survey

4.1 Introduction

The neutral hydrogen (HI) is the most abundant material in the Galaxy so that it reveals the structure of the interstellar medium (ISM), which is very complex and has chaotic motion. This complex motion of the neutral gas is mainly caused by the interstellar turbulence. In the ISM turbulence exists in from large to small scales: on galactic scales, it supports the galaxy against the global gravitational collapse, while on smaller scales it controls the star formation rate interacting with the self-gravity (e.g., Bonazzola et al. 1987[2]; Vázquez-Semadeni et al. 1995[32]).

The power spectrum (PS) of HI emission has provided a useful information of the statistical properties of the interstellar turbulence such as its slope. Based on the statistical study of Galactic HI, Crovisier and

Dickey (1983)[4] reported that the power spectrum of the HI emission has a slope comparable to that of the Kolmogorov power spectrum (Kolmogorov 1941[18]), $-5/3$, which describes the energy cascade from large to smaller scales for incompressible turbulence. In shock-dominated turbulent flows, the slope of the velocity PS is -2 , which results from the fact that the slope of Fourier transform of a step function. The power spectra of density and velocity fields of compressible turbulent flows generated in numerical simulations have been studied. One of the important findings of the previous works is that the density PS flattens with increasing rms sonic Mach number in isothermal hydrodynamic turbulent flows (Kim and Ryu 2005[15]), while the velocity PS steepens (Gazol and Kim 2010[10]).

The density probability distribution function (dPDF) has been widely used to describe the density structure of the medium. In numerical simulations with the isothermal equation state, it is well known that turbulent flows show a lognormal (LN) distribution (Vázquez-Semadeni 1994[31]; Ostriker et al. 1999 [25]; Klessen 2000[17]; Ostriker et al. 2001[26]; Li et al. 2004[22]). Several physical and environmental effects influence the lognormal dPDF; the non-isothermal equation of state generates a dPDF with a power-law tail (Passot and Vázquez-Semadeni 1998[27]; Scalo et al. 1998[30]; Nordlund and Padoan 1999[24]), magnetic fields make a dPDF with narrower dispersion (Molina et al. 2012[23]), and self-gravity of gas skews a dPDF with a power-law tail at a high-density region (Klessen 2000[17]; Dib and Berkert 2005[5]; Federrath et al. 2008[8]; Vázquez-Semadeni et al. 2008[33]; Cho and Kim 2011[3]). Furthermore, the deformed lognormal dPDF by self-gravity could enhance the star formation rate.

The neutral gas is composed of the warm and the cold neutral media (WNM and CNM), where the heating and cooling processes and thermal instability (e.g., Field, Goldsmith & Habing (1969)[9]) make the ISM more complex. In the Milky Way, the fraction of CNM and WNM is changing with the galactic latitude, where the vertical height of each medium is known to be 150 pc and 400 pc at the Sun location, respectively (see Kalberla 2003[14]). Berkhuijsen and Fletcher (2008)[1] separated the negatively skewed density PDF of the diffuse ISM into two LN-PDFs with different dispersions and positions of density peaks for the two galactic latitude ranges of $|b| < 5^\circ$ and $|b| \geq 5^\circ$, corresponding to the different states of the diffuse gas. Since then the dPDFs of the diffuse gas have been studied with a two-phase environment and along the vertical direction (e.g., Gazol and Kim 2013[11]; Gent et al. 2013[12]) through numerical simulations, but there are few studies of the Galactic HI through the observations.

In this paper, we focused on the variation of the statistical properties of Galactic HI with latitude in the statistical quantities of for the PS and PDF. Recently, the neutral hydrogen emission has been observed at the first quadrant of the Galactic plane in the Inner Galaxy Arecibo L-band Feed Array (I-GALFA) HI 21 cm line survey (Peek et al. 2010[28]; Peek et al. 2011[29]; Koo et al. 2010[19]; Gibson et al. 2012[13]). We investigated the HI position-position-velocity (PPV) cube to infer the temperature distribution as a function of the Galactic latitude from the thermal width of the density PS. We also separated the non-LN distribution of the dPDF into two LN-fitted functions which correspond to the warm and cold phase media. We, furthermore, compared the statistical properties of observational results to those of the synthetic PPV cube from a galactic-

scale numerical simulation (Kim et al. 2013[16]). From the comparison, we could see the relation between the thermal width and the PS slope.

We organize the paper in the following way. In section 2, we describe the observational data and the modification process for the statistical approach. We provide the results on the density PS and PDF in section 3. In section 4, we will discuss these results in comparison with the synthetic HI PPV cube data. In section 5, the summary will be followed.

4.2 Observations

HI emission is ubiquitous in our Galaxy and has provided useful information on the study of the Galactic structure and the kinematics of the ISM. HI emission reveals major spiral arms in our Galaxy and even provides us the distance information to the spiral arms. One of the major goals of this study is to study statistical properties of PS and PDF of turbulent HI along the Galactic latitude. For this goal, we need a high spatial resolution to get nicer statistical properties of density PS, a high-velocity resolution to investigate the thermal width, high image sensitivity to separate WNM and CNM properly, and broader latitude coverage to study the statistical properties as a function of the Galactic latitude. HI data of the Outer spiral arm from the I-GALFA HI 21 cm line survey fulfills our demands with spatial and velocity resolution of $1'$ and 0.184 km/s, image sensitivity of 0.2 K, and latitude coverage of -11 to 11° .

Figure 4.1 shows the positions of the Outer spiral arm (upper panel, arm1) and the Scutum-Centaurus arm (lower panel, arm2). The background images are (l, v) maps generated with the integration over the specific latitude regions marked at the right corner of each panel. The white dashed line on each panel shows one boundary velocity for the velocity coverage of the arm as a function of the longitude, where the brightness temperature is minimum. The yellow line at each panel is the velocity with the maximum brightness temperature at each longitude and the green and the red lines are the linearly fitted lines to each of the yellow lines. We define the Outer spiral arm within the longitude range between $l = 48^\circ$ to 68° and the velocity range between -70 at to -50 km/s, respectively. We pick up the PPV cube of the Outer spiral arm paral-

labeled to the linearly fitted line in Figure 4.1 with the velocity coverage of 13.8 km/s in which the total number of velocity channels is 75. If we pick broader velocity coverage, the cube contains the velocity component from the Scutum-Centaurus spiral arm. If we increase the longitude coverage, the HI emission of the interarm and inner Galaxy components could be included.

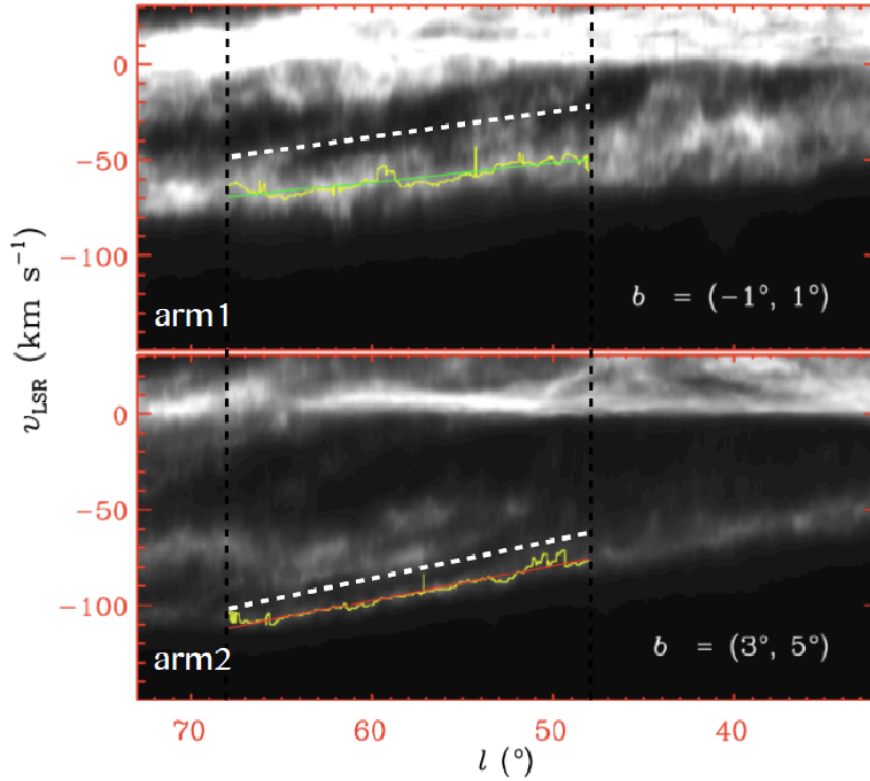


Figure 4.1 The integrated (l, v) maps and the positions of the Outer spiral arm (upper panel, arm1) and the Scutum-Centaurus spiral arm (lower panel, arm2). The latitude range for integration is shown at the right corner of each panel. The background gray contour images are the integrated brightness temperature. We are interested in HI emission below the white dashed line in each panel. The white dashed line on each panel shows one boundary velocity for the velocity coverage of the arm as a function of the longitude, where the brightness temperature is minimum. The yellow line at each panel is the velocity with the maximum brightness temperature at each longitude and the green and the red lines are the linearly fitted lines to each of the yellow lines.

Figure 4.2 shows the brightness temperature distribution averaged over each axis of the PPV cube. With the kinematic distances to the velocity centers at the leftmost longitude $l = 68^\circ$ and the rightmost longitude $l = 48^\circ$ being about 16 kpc and 14 kpc, respectively, we convert the degree units of the longitude and the latitude into the real size, kpc unit. Levine and Heiles (2006)[21] calculate the shape of the warp of the Galactic outer disk, which is drawn in Figure 4.2 with the red dashed line. We, independently, measure the brightness temperature weighted midplane, $Z_0(x)$, and the scale height, $H_T(x)$, at each longitude with the following equations:

$$Z_0(x) = \frac{\int z T_b(x, z) dz}{\int T_b(x, z) dz}, \quad (4.1)$$

$$H_T(x) = \left[\frac{\int z^2 T_b(x, z) dz}{\int T_b(x, z) dz} \right]^{1/2} \quad (4.2)$$

where $T_b(x, z)$ is the brightness temperature distribution along the longitude (x -) direction and latitude (z -) directions shown in the upper left panel of Figure 4.2. The central solid red line in Figure 4.2 calculated using equation (4.1) is slightly lower than the midplane defined by Levine and Heiles (2006)[21]. The other six red solid lines denote $-3H_T(x)$, $-2H_T(x)$, $-H_T(x)$, $H_T(x)$, $2H_T(x)$, and $3H_T(x)$ calculated using equation (4.2). Thirty-six (6×6) rectangular regions with a size of 0.5 kpc (2°) at each side are chosen between the red lines to investigate two-dimensional PS and PDF along the vertical distance. In order to study the boundary effect, we pick up the small PPV cubes or PP integrated maps at a rectangular region shown as a dashed yellow line, which is twice larger in size than the regions of interest. Under the assumption of the optically thin approximation, the integrated brightness temperature is proportional to the column density of HI along with a line-of-sight. Hereafter, we some-

times call the integrated brightness temperature as the column density, or simply density. In the upper right panel, the bv-map shows the tilted distribution of the density. The lower side of the arm is broader than the upper side. A solid line in Figure 4.3 shows the distribution of the longitude-averaged brightness temperature as a function of the latitude and a dashed line is its Gaussian fitting. The peak position is around 0.3 kpc above the midplane. We could see a negatively skewed distribution with the solid line compared with the Gaussian fitting seen in the bv-map in Figure 4.2.

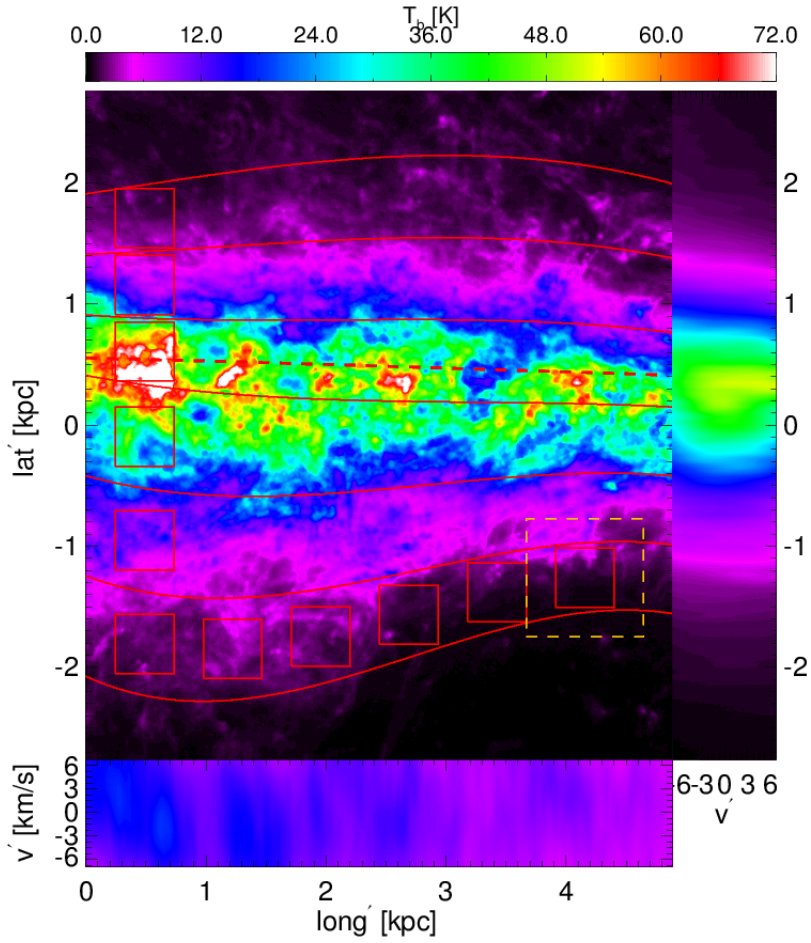


Figure 4.2 The lbv-map for the brightness temperature distribution averaged over the velocity channels (upper left panel), the longitude (upper right panel), and the latitude (lower). Each axis of the lb-map is converted into a real scale, and the color bar follows the rainbow color table which is modified to highlight the diffuse medium with bright purple color. The dashed line represents the position of warped Galactic midplane (Levine and Heiles (2006)[21]). The brightness temperature weighted midplane is drawn by the central red solid line. The other six red solid lines are heights with equal scale heights of $\pm H_T$, $\pm 2H_T$, and $\pm 3H_T$. The solid squares with the size of one side 0.5 kpc are the regions of interest for the statistical analyses. To see the effect of boundary condition, we select a square drawn with a dashed yellow line.

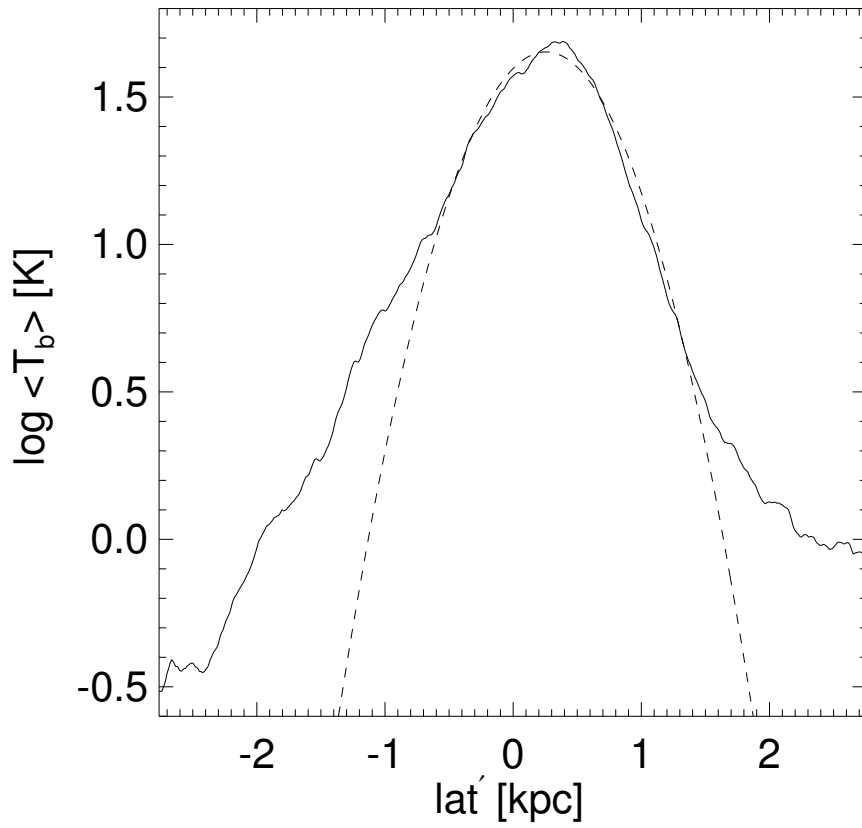


Figure 4.3 Logarithm of longitude-averaged brightness temperature as a function of the latitude direction. A solid line comes from observations and the dashed line is its Gaussian fitting.

4.3 Results

4.3.1 Density Power Spectra

Power spectra of the brightness temperature distributions integrated with different velocity widths are calculated. At first, we take the average of power spectra with a certain velocity range of Δv , where the width is varied from 1.84 to 13 km/s. Then, the power averaged spectra are calculated for all the 36 regions and the different velocity widths. Finally, the average power spectra and also the slopes of the power spectra are averaged again. Spectra index is measured in the inertial range, $3 \leq kL \leq 10$, shown with the dashed lines in the left panel of Figure 4.4.

The right panel of Figure 4.4 shows the slopes of the averaged power spectra with the velocity width. The slopes are changing slightly with the velocity width and the latitude, even though we can hardly recognize the difference between the slopes of power spectra in the left panel. The slopes of power spectra vary from around -1.8 to -2.0. The spectral index becomes the steepest at the lower latitude (red line) but flattens at the higher latitude (black line). At the lower latitude, the spectral slopes of the power spectra increase with increasing the velocity width from 1.84 km/s to 5.5 km/s. This is due to the fact that the small-scale structures within the larger velocity width are overlapped with each other to become a larger-scale structure. Lazarian and Pogosyan (2000)[20] describes the nature of the steepening of the power spectra with increasing velocity width. They argue that the steepening will continue up to a point, where the velocity width, Δv , is 3.5 times of the thermal width, v_T , of the ISM. We can convert the condition into the following equation, $T \simeq 15(\Delta v[\text{km s}^{-1}])^2$, where T is the temperature of the HI gas and $\Delta v[\text{km s}^{-1}]$ is the

velocity width measured in units of km s^{-1} . From the spectral slopes in the right panel of Figure 4.4, the turning points occur at the velocity widths of 5.5 km s^{-1} for the red line, 9 km s^{-1} for the blue line, and larger than 13 km s^{-1} for the black line, which correspond to the temperatures of 450 K, 1200 K, and $\geq 2500 \text{ K}$. The temperatures estimated with the steepening condition are consistent with the temperatures of the dominant phases of HI gas at different latitudes. For example, the cold neutral medium (CNM) would be mostly concentrated at the low latitude. Its temperature is around 100 K, which is quite similar to 450 K estimated by the steepening condition. If a velocity width is larger than the velocity width with the maximally steepened spectral index, then power spectra flatten as shown in Figure 4.4 because of the increased power of small scale structure. It could occur due to the contamination near at the edge of the velocity width from inter-arms or neighboring spiral arms. Or energetic events such as supernova explosions blow the gas away beyond the edge of the velocity width. For the latter possibility, we will compare the power spectra obtained from synthetic and observed HI cubes.

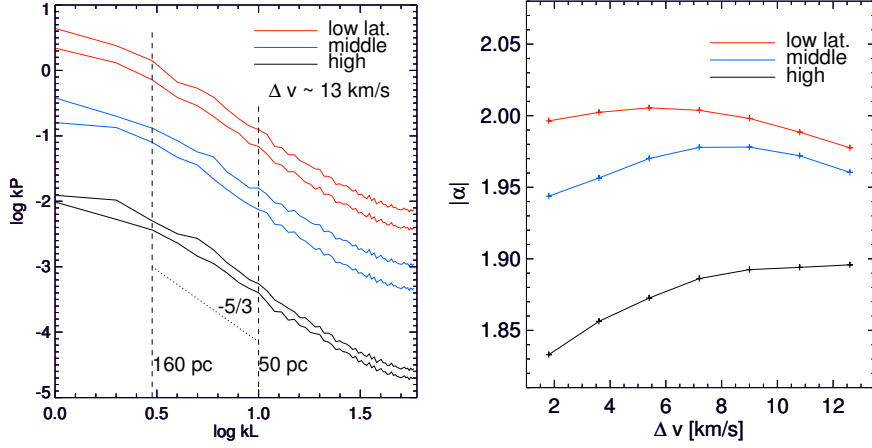


Figure 4.4 Averaged power spectra of brightness temperature distributions integrated with the largest velocity width of 13 km/s in the rectangular regions at three different latitudes (left) and the spectral slopes of brightness temperature distributions as a function of the integration velocity widths (right). In the left panel, the power spectra are shown by solid lines at three vertical distances from the midplane, which are colored in red (low latitude), blue (middle), and black (high latitude). The slopes of the power spectra are measured at the spatial range of $3 \leq kL \leq 10$ represented by the dashed lines in the left panel. For a comparison purpose, a dotted line represents of the slope of the Kolmogorov turbulence, $-5/3$. In the right panel, the same colors of the solid lines have been used to represent difference latitudes as in left panel.

Figure 4.5 shows the one-dimensional profiles in black lines at low latitude and their Gaussian fits in red. From the velocity profiles, the dispersions σ_v are written to be around 10 km/s. Considering the temperature of 450 K and the thermal velocity, $v_T = 1.6$ km/s from Figure 4.4, sonic Mach number would become $\sqrt{3}\sigma_v/v_T$ to be around 11, roughly. Because CNM is concentrated at this low latitude, most of HI of the Outer spiral arm near the midplane is in a supersonic state. Since the bulk motion of the Outer spiral arm would make the dispersion wider, the sonic Mach number of 11 is an upper limit of interstellar turbulence near the midplane.

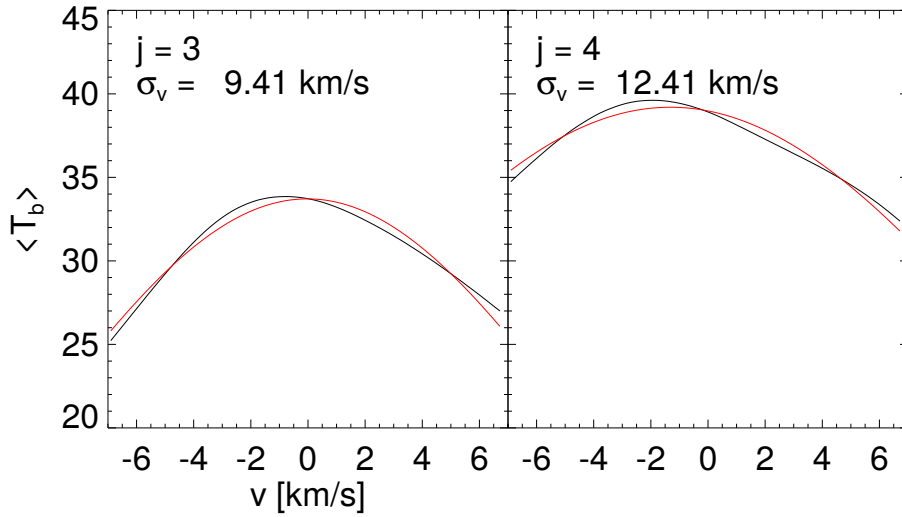


Figure 4.5 One-dimensional velocity profiles (black lines) and their Gaussian fits (red lines) at the lower latitudes. The numbers $j = 3$ and $j = 4$ indicate the two rectangular boxes at the lower latitudes shown in Figure 4.2. The brightness temperatures are averaged along the x - and z -axes at each rectangular regions. The velocity dispersion is written at the top of each panel.

4.3.2 Density Probability Distribution Function

We calculate PDFs of integrated brightness temperatures in all the 36 regions shown in Figure 4.2. First, we integrate the brightness temperature along the velocity axis. And we divide the two-dimensional integrated brightness temperature distribution by a mean of the two-dimensional plane in each region. Finally, we obtain a PDF of the integrated brightness temperature using six regions at the same latitude. Figure 4.6 shows the volume-weighted PDFs of integrated brightness temperature with latitude. The j -value in each panel represents different latitude: $j=3, 4$ (low latitude), $j=2, 5$ (middle latitude), and $j=1, 6$ (high latitude). The dispersions of each PDFs are nearly similar to each other. In the higher latitude, Type Ia supernovae (SNe) might be an energy source for the wide dispersion since the scale height is over \sim kpc. Because the density of the medium is very rarefied at higher latitude, the supernova remnants (SNRs) evolve very slowly to maintain the wide PDF for a long time. In the lower latitude, though SNe explode much frequently, the SNRs evolve very fast since the density of the ISM is much denser.

The PDFs do not follow a lognormal distribution but are skewed negatively at $j=3, 4$ or positively at the higher latitude. If we assume a two-phase medium, we can separate these PDFs into two LN-functions for CNM (blue lines) and warm neutral medium (WNM; red lines). The negative skewness at low latitudes is due to the contribution of the WNM while the positive skewness, even though it is small, is due to the small contribution of CNM.

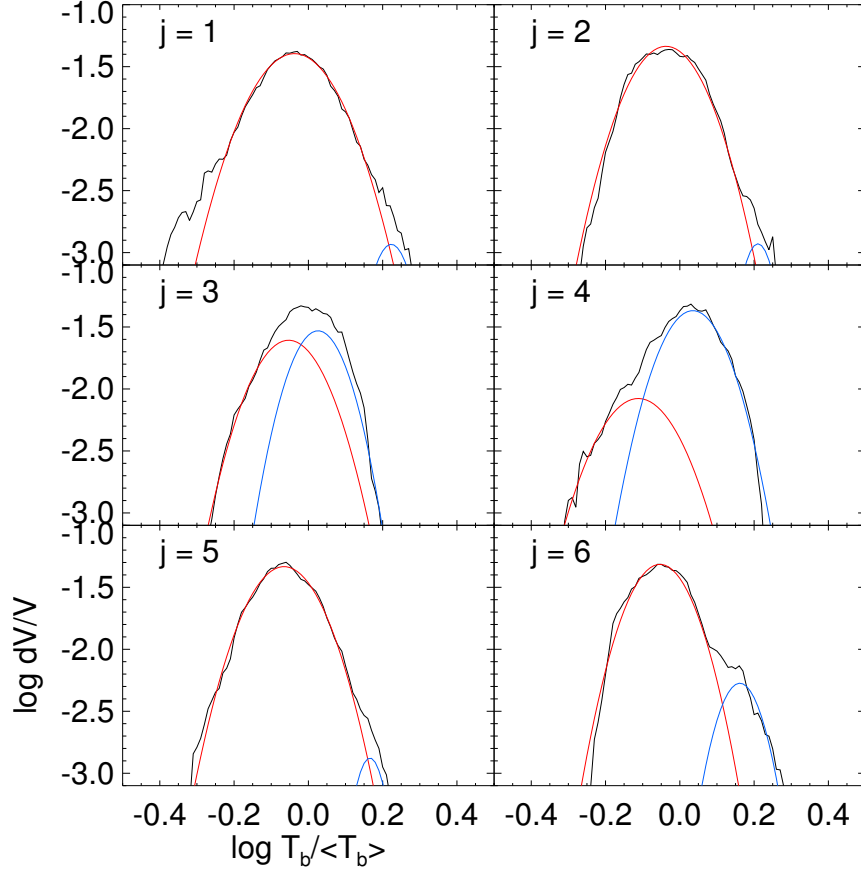


Figure 4.6 Probability density function of the integrated brightness temperature at different latitudes. Solid lines are from observations and red and blue lines are log-normal fittings. The number j in each panel starts from 1 at the negative higher latitude to 6 at the positive higher latitude (see Figure 4.2). Notice the cold gas (blue line) is comparable to the warm gas (red line) near the Galactic midplane in the panels of $j = 3$ and 4.

The panel labeled with $j=1$ shows that the PDF has a little bump at the lower brightness temperature region. As mentioned above, since the bright temperature weighted midplane drawn in Figure 4.2 is above $b = 0$, the brightness temperature distribution at the region of $j=1$ at the higher latitude of the lower hemisphere shows a noisy pattern. So the bump at the lower brightness region in the panel $j = 1$ would be meaningless. The scale height of WNM is just 150 pc at the Sun site, and it could increase at the outer Galaxy, because of lower gravitational attraction from the stars and dark matters at the Galactic disk. But the spatial interval between the rectangular regions of interest equals one density-weighted scale height, which roughly exceeds 500 pc. So the transition of the fraction of CNM looks very rapidly. In the panel labeled with $j=6$ (higher latitude in the upper hemisphere), the fraction of CNM is quite high. This is because there are the several faint HI clouds on the panel.

The dispersions of the PDFs even at the different latitude are similar each other, which could not be explained by the numerical simulations shown in the previous chapter. We could consider the distribution of the kinetic energy injector. Since the scale height of the thick disk in the Milky Way is around one kpc, SNIa could be placed at a kpc height. The previous numerical simulations include only the supernova explosions from massive progenitors. Also, the effect of the magnetic field could be considered. If the galactic magnetic field strength is roughly assumed to be more strong near the plane of the galaxy than that in the higher latitude, the magnetic field might narrow the dispersion of the density PDF at low altitude. Moreover, in the outer galaxy, turbulent energy injection in the galactic scale becomes more important than that from stellar sources so it might be difficult to see the difference between the density PDFs

with different latitudes. In future work, we could investigate the density PDF with latitude in numerical models for interstellar turbulence in the stratified ISM, including the galactic magnetic field.

4.4 Power Spectra from a Synthetic HI PPV Cube

4.4.1 Numerical Simulations

We use hydrodynamic (HD) numerical models of Kim et al. (2013)[16] to make a comparison of the numerical model with the I-GALFA observation. The models cover relatively higher latitude, include realistic physical ingredients such as self- and external gravity to make a stratified large-scale structure of the ISM, drive the realistic turbulence from SN explosions. Among them, we select a model, QA05, since the surface density of the model, $5 M_{\odot} \text{ pc}^{-2}$, is close to the Outer spiral arm. In brief, we introduce some of the numerical parameters of QA05 we use in this paper. t_{orb} is the orbital period, $t_{\text{orb}} \equiv 2\pi/\Omega = 220\text{Myr}(\Sigma/10M_{\odot}\text{pc}^{-2})^{-1}$, where the galactic rotational speed varies as $\Omega = 28\text{kms}^{-1}\text{kpc}^{-1}(10M_{\odot}\text{pc}^{-2}/\Sigma)$ to keep the gaseous Toomre Q parameter constant. The horizontal domain sizes are $L_x = L_y = 512 \text{ pc}$, and the resolution of each grid is fixed by 2 pc in all models. The vertical size, L_z , is set to be 1024 pc to cover at least two scale height of two-phase gas. And the thermal velocity dispersions is about 3.85 km/s. Detailed descriptions for the numerical models such as the driving mechanism of turbulence and other physical ingredients are provided in the paper of Kim et al. (2013)[16].

4.4.2 Slopes of Power Spectra of the Synthetic Cubes

We make synthesized PPV cubes from the numerical model to compare its result to that of the I-GALFA observation. The absorption coefficient of the HI 21 cm line is shown below: (e.g., Draine 2011[7]):

$$\kappa_{\nu} = \frac{3}{32\pi} \frac{3}{\sqrt{2\pi}} \frac{A_{ul}\lambda_{ul}^2}{\sigma_V} \frac{hc}{kT_s} e^{-u^2/2\sigma_V^2} n(\text{HI}), \quad (4.3)$$

where A_{ul} is the Einstein A coefficient, λ_{ul} is the wavelength of 21 cm, σ_V is the Doppler width of the line - we set this the adiabatic sound speed of the medium. We assume that each grid point of the cube emits a Gaussian HI 21 cm line profile with thermal width at T_s :

$$T_s = \frac{T_R + xT_k}{1 + x}, \quad (4.4)$$

where $T_R = 3.77$ K is the brightness temperature of the background 21 cm radiation field, and T_k is the kinetic energy, and $x = n(\text{HI})\Delta E_{21}q_{21}/A_{21}kT_k$ could be approximated to $x \simeq 240n(\text{HI})/\sqrt{T_k}$. Then we got the optical depth with integrating the absorption coefficient κ_ν through the line of sight. For simpler approach, we assumed the PPV cube is optically thin to neglect the higher density, $n(\text{HI}) > 50 \text{ cm}^{-3}$, then the optical depth could be described in the following,

$$\tau_\nu = 2.190 \frac{N(\text{HI})}{10^{21} \text{cm}^{-2}} \frac{100 \text{K kms}^{-1}}{T_s} \frac{1}{\sigma_V} e^{-u^2/2\sigma_V^2}. \quad (4.5)$$

Finally, integrating the T_s for the all optical depth would give the brightness temperature,

$$T_b = \int_0^\infty T_s(r) \exp[-\tau(V, r)] d\tau \quad (4.6)$$

Figure 4.7 is the averaged images of a brightness temperature PPV cube, which comes from the snapshot of the numerical simulation at $t/t_{orb} \simeq 1.5$, when supernova remnants (SNRs) are pushing the ISM into the halo. The upper right and lower panels share the same color bar in the left top of the figure. In the (x, z) plane, the HI distribution shows quite diffuse and small-scale structure. There are two expanding SNRs colored red and yellow on the right middle side of the upper left panel. Following the red dashed lines to the right panel shown in the (v, z) plane, the width

of the velocity is enormous at the positions of the expanding SNRs. Also in the bottom panel, the two SNRs show wide velocity coverage.

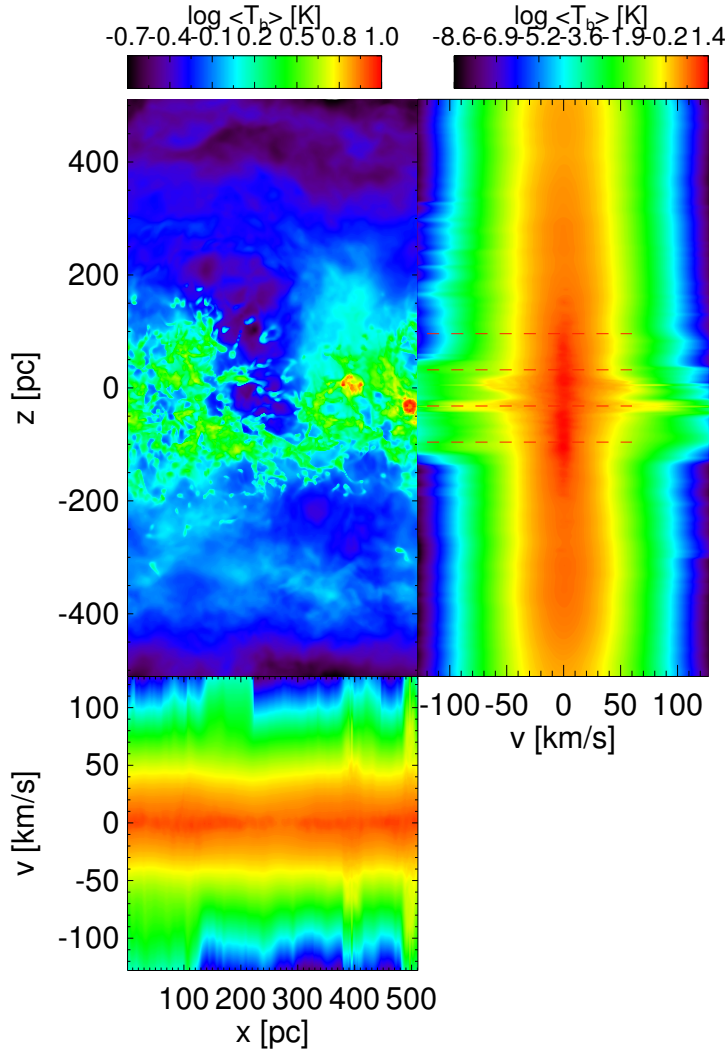


Figure 4.7 Brightness temperature maps from the synthetic HI PPV cube from a numerical model. Averaged brightness temperature maps are shown in (x, z) plane at the upper left panel, (v, z) plane at the upper right panel, and (x, v) plane in the lower panel. The v , x , and z present the velocity channel, a local coordinate in the direction parallel to a spiral arm, and vertical coordinate parallel to the midplane, respectively. The color bar above the (v, z) is shared with the lower panel.

Figure 4.8 shows the variation of the slope of integrated brightness temperature distributions from the synthetic PPV cube as a function of velocity channel width. The observational counterpart of Figure 4.8 is the right panel of Figure 4.4. The blue and red lines represent the slope variation near the midplane and higher latitude, respectively. Again, in Figure 8, we could see the steepening of the spectral slope up to around 12 to 15 km s⁻¹ velocity width. Beyond the 12 km s⁻¹ velocity width, the spectral slope (red line) hardly changes at the higher latitude, while the spectral slope near the midplane flattens beyond the 15 km s⁻¹ velocity width (blue line) in Figure 4.8. The counterpart of the blue line in Figure 4.8 is the blue line in the right panel in Figure 4.4. We could see the flattening nature of the spectral slope beyond the thermal velocity width in both observational and synthetic H I data cubes. From the maps in Figure 4.7 from the synthetic HI PPV cube, we could clearly see that the flattening nature beyond the velocity width of ~ 15 km/s is due to active energy injection by SN explosions. The width of the velocity, 15 km/s is converted into 3300 K, which correspond to the mean value of temperature over the latitude, 3800 K. The energy injection sends the HI gas to the outskirts and induces a very broad dispersion of a velocity field, which makes the spectral power of the small scale turbulent structure rise, and the spectral slope flatten.

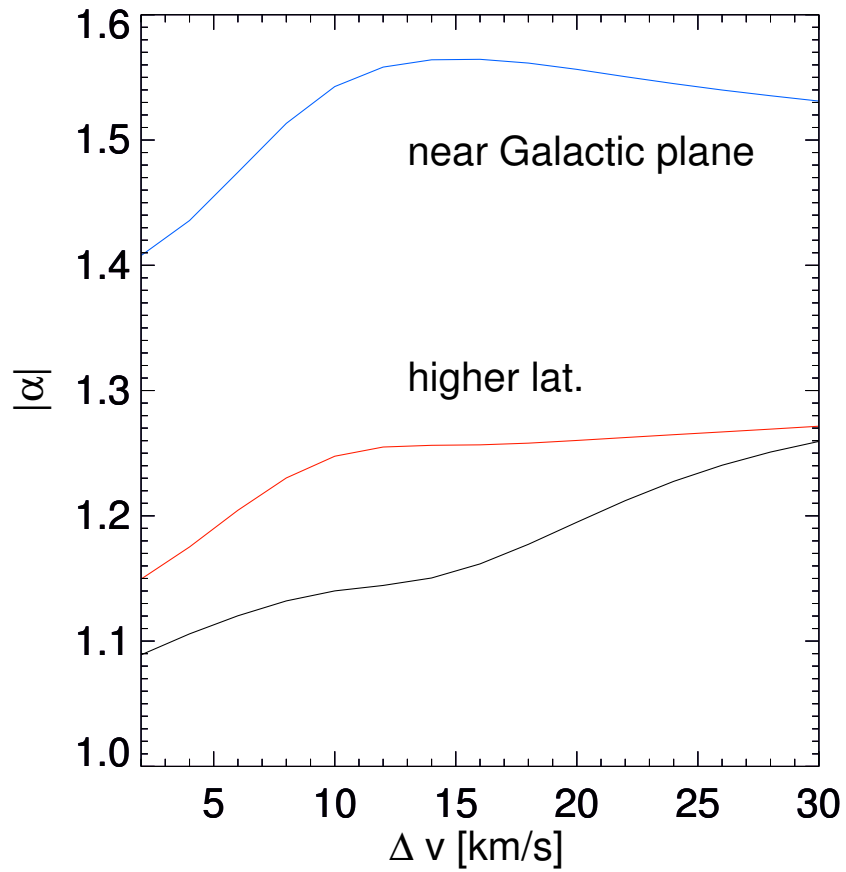


Figure 4.8 Slopes of the power spectra at the different latitudes of the synthetic HI PPV cube as a function of the velocity width. In the previous figure, the red dashed lines denote the region of interest. The blue line represents the slope of the power spectrum at the Galactic disk.

4.5 Summary

We analyzed the HI structure in the Outer Spiral arm from the I-GALFA HI 21 cm line survey, which has a high spatial and velocity resolution, high image sensitivity, and broad latitude coverage to study the statistical turbulence properties of the arm as a function of the Galactic latitude. We select the Outer arm region distributed the longitude range between $l = 48^\circ$ to 68° . We also select 75 velocity channels covering 13.8 km/s parallel to the linearly fitted line to the positions of maximum brightness temperature on the (l,v) map of the Outer arm (see Figure 4.1). The longitude angle is converted to the real size considering the fact that the distance to the arm at $l = 68^\circ$ is about 16 kpc and it is 14 pc at $l = 48^\circ$. Following the density weighted midplane and scale height, we finally picked up 6x6 rectangular regions for the analyses of PDFs and PS (see Figure 4.2).

The slope of power spectra of brightness temperature distributions becomes steep as the velocity width increases up to the thermal velocity width. This is because the small-scale structures are overlapped each other to enhance the power at larger scales. Beyond the thermal velocity width, the spectral slope flattens especially in the lower latitude, which is contradictory to the expectation of Dickey et al. (2001)[6]. This could be caused by the energy injection by SNRs (see Figure 4.4). We discussed the synthetic snapshot of a numerical model, QA05, of Kim et al. (2013)[16], which includes realistic conditions for the stratified Galactic thick disk such as self- and external gravity, cooling and heating processes, SN energy injection, and galactic differential rotation. In the numerical model, we could find that the slope would rise and fall with young SNRs near the

Galactic midplane like our observational results. The young SNRs could blow the HI gas from the velocity center to make the slope flatten. But in the Outer arm region, the small-scale structures with different velocity range like interarm or neighbor arms could contaminate the velocity edge such that the spectral slope to be flattened.

We calculate the volume-weighted probability distribution functions (PDFs) of integrated brightness temperature distribution in all the 36 regions. The PDFs don't follow a lognormal distribution but are skewed negatively or positively at different latitudes. We separate the skewed PDFs into two LN-functions, then we interpret the skewness with a two cold and warm gas components. The skewness of PDF is negative due to the warm neutral gas at the lower latitude, while it is positive due to the cold neutral gas at the higher latitude.

Bibliography

- [1] Berkhuijsen, E., & Fletcher, A. 2008, MNRAS, 390, 19
- [2] Bonazzola, S., Heyvaerts, J., Falgarone, E., Perault, M., & Puget, J. L., 1987, A&A, 172,293
- [3] Cho, W., & Kim, J., 2011, MNRAS, 410, 8
- [4] Crovisier, J. & Dickey, J.M., 1983, 122, 282.
- [5] Dib, S., & Burkert, A., 2005, ApJ,630, 238
- [6] Dickey, J. M., McClure-Griffiths, N. M., Stanimirović, S., Gaensler, B. M., & Green, A. J., 2001, ApJ, 561, 264
- [7] Draine, B. T., 2011, Physics of the Interstellar and Intergalactic Medium (Princeton, NJ: Princeton Univ. Press)
- [8] Federrath, C., Klessen, R. S., & Schmidt, W. 2008, ApJ, 688, 79
- [9] Field, G. B., Goldsmith, D. W., Habing, H. J. (1969), ApJ, 155, L149
- [10] Gazol, A. & Kim, J., 2010, ApJ, 630, 911
- [11] Gazol, A. & Kim, J., 2013, ApJ, 765, 49

- [12] Gent, F. A., Shukurov, A., Sarson, G. R., Fletcher, A., & Mantere, M. J. 2013, MNRAS, 435, 689
- [13] Gibson, S. J., Koo, B., Douglas, K. A., et al. 2012, BAAS, 219, 349.29
- [14] Kalberla P. M. W., & Kerp, J., 2009, ARAA, 427, 27 L45
- [15] Kim, J., & Ryu, D. 2005, ApJ, 630, L45
- [16] Kim, C-G., Ostriker, E. C., & Kim, W-T 2013, ApJ, 776, 1
- [17] Klessen, R. S., 2000, ApJ, 535, 869
- [18] Kolmogorov, A. 1941, DoSSR, 30, 301
- [19] Koo, B.-C., Gibson, S. J., Kang, J.-h., et al. 2010, HiA, 15, 788
- [20] Lazarian, A. & Pogosyan, D. 2000, 537, 720
- [21] Levine, E. S., & Heiles C., 2006, ApJ, 643, 881
- [22] Li, P. S., Norman, M. L., & Mac Low M.- M., & Heitsch, F., 2004, ApJ, 605, 800
- [23] Molina, F. Z., Glover, S. C. O., Federrath, C., & Klessen, R. S., 2012, MNRAS, 423, 2680
- [24] Nordlund, A., & Padoan, P., 1999, In Interstellar Turbulence, Proc., 2nd Guillermo Haro Conf., ed., J, Franco, A., Carraminana, pp., 218, Cambridge: Cambridge Univ. Press
- [25] Ostriker, E. C., Gammie, C. F., & Stone, J. M., 1999, ApJ, 513, 259
- [26] Ostriker, E. C., Stone, J. M., & Gammie C. F. 2001, ApJ, 546, 980
- [27] Passot, T., & Vázquez-Semadeni, E. 1998, Phys. Rev. E, 58, 4501

- [28] Peek, J. E. G., Begum, A., Douglas, K. A., et al., 2010, in ASP Conf. Ser. 438, *The Dynamic Interstellar Medium: A Celebration of the Canadian Galactic Plane Survey*, ed. R. Kothes, T. L. Landecker, & A. G. Willis (San Francisco, CA: ASP), 393
- [29] Peek, J. E. G., Heiles, C., Douglas, K. A., et al. 2011, *ApJS*, 194, 20
- [30] Scalo, J., Vázquez-Semadeni, E., Chappell, D., & Passot, T., 1998, *ApJ*, 504, 835
- [31] Vázquez-Semaceni, E., 1994, *ApJ*, 423, 681
- [32] Vázquez-Semadeni, E., Passot, T., & Pouquet, A., 1995, *ApJ*, 441, 702
- [33] Vázquez-Semadeni, E., González, R. F., Ballesteros-Paredes J., Gazol, A., & Kim, J., 2008, *MNRAS*, 390, 769

Chapter 5

Conculsion

In order to understand the multi-scale nature of interstellar turbulence, this dissertation contains numerical and observational studies on interstellar turbulence in a more realistic environment. The structures of the turbulent interstellar medium (ISM) are very complex and should have been studied statistically in both HI observations and numerics. The statistical properties of the turbulence are confirmed to be changed by the surrounding physical components and environmental influences. In this thesis, I have investigated the effects of supernova explosions, two-phase gas components, vertical stratification of the interstellar medium on the density probability distribution function (PDF) and power spectrum (PS).

First of all, the lognormality of a density PDF is one of the well-known statistical characteristics of the isothermal turbulence. The star formation rate (SFR) in a molecular cloud has been measured based on the lognormal (LN) function, where the relation between turbulence and star forming process has been an important issue in the molecular cloud.

It was, however, underestimated because the LN density PDF results from numerical simulations without self-gravity. Including self-gravity, the density PDF is skewed positively so that there is higher fraction at the high-density region. In this thesis, I have conducted a quantitative statistical analysis for the enhancement of the SFR with a three-dimensional hydrodynamic numerical simulation for interstellar turbulence with self-gravity.

Second, the statistical properties of turbulence have been altered under environmental influences. In a galactic scale, the properties could be examined along with the galactic latitude. Recently, Kim et al. (2013)[16] have performed hydrodynamic simulations with large vertical coverage to adequately describe the vertically stratified ISM, two-phase gas components, and turbulence driving by supernova (SN) explosions. In addition, the Inner Galaxy Arecibo L-band Feed Array (I-GALFA) HI 21 cm line survey provides the broad latitude coverage, high spatial and velocity resolutions, and high image sensitivity. I made density PDFs, the power spectra of velocity and density, and measured the compressibility of these numerical and observational data cubes. I also made a comparison of the statistical properties from both numerical and observational data cubes.

In chapter 2, I have done a magnetically supercritical and supersonic turbulence simulation with the isothermal equation of state to study the effects of self-gravity on density PDFs and the core formation rate. Self-gravity helps to form the extended tail of a density PDF at a high-density region, which significantly increases the core formation rate per free-fall time. The equal condition between the local Jeans and sonic lengths shows the normalized critical density by an initial density for core collapse between 31 and 48. In this range of critical density, the core formation rate (CFR) becomes 6.1 times larger than that of the LN distribution. For a

given normalized critical density of 100, the core formation rate per free-fall time becomes about 49 times larger. Self-gravity enhances the core formation rate significantly in the turbulent ISM.

In chapter 3, I present the statistics of the numerical simulations for the turbulent and stratified ISM to study density and velocity fields as a function of the vertical distance from the midplane. The dPDFs have a double-peaked shape at lower hemisphere while the dPDFs in upper hemisphere follow the lognormal distribution. The double-peaked shape was separated into two components contributed from warm and cold gas phases. To quantify the shape of dPDFs, I measured the skewness and found that it varied according to the mass fractions of the warm and cold phases at a given height. The relation of the rms sonic Mach numbers and the dispersion of density PDFs of the warm gas component in our numerical simulation is very close to the previous relationship (Ostriker et al. 2001[26]). I also showed that the volume density PDFs and column density PDFs are tightly related to each other. From the calculations of the power spectra of density and velocity as a function of the vertical height, I found that the density power spectra steepen with increasing height while the velocity power spectra become flatten. I also separated a velocity field into compressive and solenoidal components and found that the power of the solenoidal component decreases more slowly at smaller scales than that of the compressible component. On a sliced horizontal plane of a three-dimensional compressibility cube, an SN explosion is shown to be a source for generating the strong compressive velocity component. At the same time, the solenoidal velocity component is shown to be caused by the curved shock near the SNR. I also proposed a new easy method to measure velocity compressibility in real space, which will be

very useful for future study on turbulence. As a future work, I will apply the same statistical methods that have been used in these to the numerical models which include more realistic physical ingredients such as magnetic fields and hot medium over the wide range of Mach numbers.

In chapter 4, I showed the statistical study of HI distribution in the Outer Spiral arm from the I-GALFA HI 21 cm line survey. I selected 36 regions in the Outer arm region distributed in the longitude range between $l = 48^\circ$ to 68° and between $b = \pm 11^\circ$. To minimize the contamination of the HI from interarm and neighbor arm, I picked up 75 velocity channels covering 13.8 km/s parallel to the linearly fitted line to the positions of maximum brightness temperature on the (l, v) map of the Outer arm. In those regions, the slope of power spectra of brightness temperature distributions becomes steeper as the velocity width increases up to the thermal velocity width. This is because the small-scale structures are overlapped each other to enhance the power at larger scales. Beyond the thermal velocity width, the spectral slope flattens especially in the lower latitude, which is contradictory to the expectation of Dickey et al. (2001)[6]. From the synthetic snapshot of a numerical model, the slope would rise and fall with young SNRs near the Galactic midplane like our observational results. The young SNRs could blow the HI gas from the velocity center to make the slope flatten. But in the Outer arm region, the small-scale structures with different velocity range like interarm or neighbor arms could contaminate the velocity edge such that the spectral slope to be flattened. The PDFs of integrated brightness temperature distribution don't follow a lognormal distribution but are skewed negatively or positively at different latitudes. I separated the skewed PDFs into two LN-functions and concluded that the skewness of PDF is negative due to

the warm neutral gas at the lower latitude, while it is positive due to the cold neutral gas at the higher latitude.

초록

난류는 성간 매질에서 어디에나 존재하는 중요한 물리 인자 중 하나이다. 작게는 AU 규모에서 크게는 kpc 규모까지 다양한 범위에서 성간 매질의 진화에 결정적인 역할을한다. 성간 난류의 다중 규모 특성을 이해하기 위해서, 수치 실험 뿐 아니라 관측 연구에서도 성간 난류의 통계적 특성에 대한 연구가 필요하다. 수치 계산은 성간 난류의 동역학을 이해할 수 있는 유일한 방법으로, 여러 다양한 규모와 다양한 환경에서 난류가 심한 성간 매질의 진화를 이해하는데 필수적이다. 또한 관측 연구에서는 통계 연구를 바탕으로, 다양한 규모에서 일어나는 성간 난류의 변화를 한 눈에 볼 수 있도록 해 준다. 이 논문에서 나는 분자운 규모 혹은 은하 규모에서 펼쳐지는 성간 난류의 진화에 대한 관측과 수치 연구를 동시에 수행했다. 이를 위해 필자는 난류의 통계 분석을 위해, 기존에 잘 알려진 두 가지 방법인 확률 밀도 함수와 파워 스펙트럼을 사용했다. 등은 환경 또는 비압축성인 이상적인 환경에서, 각각 로그 정규 분포와 Kolmogorov 파워 스펙트럼이라는 대표적인 분포를 예상할 수 있다.

첫 번째 장에서, 난류와 자기 중력에 영향을 받는 분자운내 별핵 생성율에 대하여 정량적으로 논의하였다. 자기 중력, 초음속 성간 난류, 자기장을 포함한 수치 실험에 대하여 밀도의 확률 분포 함수를 구하였다. 성간 난류의 밀도 구조는 자기 중력에 의해 로그 정규 분포로부터 벗어난다. 자유 낙하 시간 동안의 별핵 생성율을 조사해 본 결과, 별핵생성율은 자기 중력과 함께 급격한 증가를 보인다. 초기 평균 밀도의 100 배를 별핵 생성의 한계 밀도라고 할 때, 자기 중력 영향 아래에서 별핵 생성율은 로그 정규 분포를 가정했을 때에 비해 49배 정도 높다. 따라서 로그 정규 분포를 가정하여 별핵 생성을 즉 별핵 질량 함수를 구해 왔던 이전 연구는, 이제 자기 중력을 고려하는 방

향으로 수정되어야 할 것이다. 별 생성이 활발한 분자운들을 관측해 보았을 때 높은 밀도 영역에서 밀도의 확률이 로그 정규 분포에서 주어진 확률에 비해 큰 점을 들어, 이러한 주장은 관측 연구에 있어서도 합리적이라고 할 것이다.

두 번째 장에서는 은하 평면으로부터 서로 다른 수직 거리에 분포하는 층화된 난류성 성간 매질의 성질을 이해하기 위하여, 은하 규모에서 수행된 수치 모델에 대한 통계 분석을 제시한다. 은하 평면 근처에서 밀도 확률 분포 함수는 로그 정규 분포로부터의 편차를 나타내는 이중 피크 분포를 보여준다. 이 이중 피크 분포는 성간 매질의 차갑고 따뜻한 기체 성분 때문이다. 각 기체가 밀도 가중 높이에 의해 표준화 된 높이로 준 질량 보존되어 있다고 가정한다면, 각 기체의 밀도 확률 분포 함수는 로그 정규 분포로 나타낼 수 있다. 은하 평면으로부터 더 높은 위치에서는, 따뜻한 기체가 대부분이고, 그 밀도 확률 분포 함수는 로그 정규 분포에 잘 맞다. 높은 곳으로 갈수록 밀도 파워 스펙트럼은 $-5/3$ 로 점점 급해지고, 속도 파워 스펙트럼 $-5/3$ 에서 점점 편평해진다. 속도 필드가 압축성 성분과 비압축성 성분으로 나뉘어 질 때, 비압축성 성분의 PS는 압축성 성분의 PS와 비교하여 평탄하다. 본 연구에서는 속도 장의 압축 정도를 시각화하는 새로운 방법을 고안하였고, 이를 위해 속도계의 발산 및 쪼를 실제 공간에서 직접 계산하였다. 초신성과 같은 강력한 폭발 현상은 강한 압축 난류를 일으킬 것으로 예상되어왔는데, 압축성을 시각화하는 방법으로부터, 비압축성 성분 또한 초신성 잔해 근처에서 휘어진 충격파에 의해 유발될 수 있다는 것을 알 수 있었다.

세 번째 장에서, I-GALFA HI 21 cm 서베이 관측 자료를 사용하여 the Outer spiral arm에 분포한 중성 수소로부터 난류성 성간 매질에 대한 연구를 제시한다. 적분한 밝기 온도의 파워 스펙트럼을 조사해 보면, 높은 은위의 기울기보다 ($\alpha \sim -1.8$) 낮은 은위의 기울기가 더 급하다 ($\alpha \sim -2$). 은하 평면 근처에서, 기울기의 변화는 속도 채널의 두께에 따라 서서히 증가하다가 열적 속도 폭에 도달하면 다시 떨어진다 (-1.97). 이러한 기울기의 변화를 이

해하기 위해, I-GALFA 관측 결과와 수치 계산 모형을 비교한다. 표면 밀도가 유사한 수치 계산 모형으로부터 중성 수소 PPV 큐브(position-position-velocity cube) 데이터를 합성하였다. 이로부터 젊은 초신성 잔해의 영향이 적분한 밝기 온도의 파워스펙트럼 기울기의 변화를 유발하는 한 가지 가능성일 수 있다는 것을 알게 되었다. 적분된 밝기 온도의 확률 분포 함수는 로그 정규 분포에 잘 맞지 않았다. 은하 평면 근처에서는 음으로 기울어져 있고, 높은 은위로 갈 수록 양으로 기울어져 간다. 각 확률 분포 함수는 두 개의 로그 정규 분포로 잘 나뉘지는데, 각각은 중성 수소의 차갑고 따뜻한 성분을 대표한다고 볼 수 있었다.

주요어: 성간 난류 — 성간 물질: 분자운 — 성간 물질: 수소 원자 — 성간 물질: 동역학 및 운동학 — 성간 물질: 구조 — 별: 생성 — 은하: 구조 — 방법: 수치 계산 — 유체 역학 — 자기 유체 역학 — 방법: 통계 — 전파 자료: 성간 물질

학번: 2006-30123